Imaging of the electrical activity in the root zone under limited water availability stress: A laboratory study for *Vitis vinifera*.

Benjamin Mary[1,2], Veronika Iván[1], Franco Meggio[3,4], Luca Peruzzo[1,2], Guillaume Blanchy[5], Chunwei Chou[2], Benedetto Ruperti[3,4], Yuxin Wu[2], Giorgio Cassiani[1]

[1]Dipartimento di Geoscienze, Università degli Studi di Padova, Padova, Italy

[2]Earth and Environmental Sciences Area, Lawrence Berkeley National Laboratory, California, USA

[3]Department of Agronomy, Food, Natural resources, Animals and Environment – DAFNAE, University of Padova, Agripolis, Viale dell'Università 16 – Legnaro (Padova), Italy;

[4]Interdepartmental Research Centre for Viticulture and Enology - CIRVE, University of Padova, Via XXVIII Aprile 14, Conegliano (Treviso), Italy;

[5]Urban and Environmental Engineering, University of Liège (ULiege), Liège, Belgium

Correspondence to: B. Mary (benjamin.mary@unipd.it)

Abstract

Understanding root signals and their consequences on the whole plant physiology is one of the keys to tackling the water-saving challenge in agriculture. The implementation of water-saving irrigation strategies, such as the partial root-zone drying (PRD) method, as part of a comprehensive approach to enhance water use efficiency. To reach this goal tools are needed for the evaluation of the root's and soil water dynamics in time and space. In controlled laboratory conditions, using a rhizotron built for geoelectrical tomography imaging, we monitored the spatio-temporal changes in soil electrical resistivity (ER) for more than a month corresponding to 8 alternating water inputs cycles. Electrical Resistivity Tomography (ERT) was complemented with Electrical Current Imaging (ECI) using plant stem-induced electrical stimulation. To estimate soil water content in the rhizotron during the experiment, we incorporated Archie's law as a constitutive model. We demonstrated that under mild water stress conditions, it is practically impossible to spatially distinguish the limited water availability effects using ECI. We evidenced that the Current Source Density spatial distribution varied during the course of the experiment with

25   the transpiration demand but without any significant relationship to the soil water content changes . On the other hand, ERT

26   showed spatial patterns associated with irrigation and, to a lesser degree, to RWU and hydraulic redistribution. The

27   interpretation of the geoelectrical imaging with respect to root activity was strengthened and correlated with indirect

28   observations of the plant transpiration using a weight monitoring lysimeter and direct observation of the plant leaf gas

29   exchanges.

30   **1.   Introduction**

31   In the context of water scarcity, agriculture needs to improve irrigation practices by reducing water inputs and selecting

32   adequate species and, in the case of woody crops, most efficient scion-rootstock combinations. In order to evaluate the

33   efficacy of irrigation, it is necessary to develop tools capable of evaluating root functioning and quantifying root water

34   uptake. The partial root zone drying (PRD) and RDI (Regulated Deficit Irrigation) methods are part of an ensemble of dificit

35   irrigation (DI) strategies that aim at improving water use efficiency. The PRD, for instance, consists of irrigating only one

36   part of the root system of the same plant using a certain percentage of the potential evapotranspiration (ETp), usually inferior

37   to the total water needed. Application of DI triggers a physiological response in the plant via a hormone called Abscisic acid

38   (ABA), which is produced in the roots and transmitted to the leaves to regulate the stomata closure and thus reducing water

39   transpiration while keeping photosynthesis active and finally leading to increased water use efficiency (as reviewed in

40   Loveys et al., 2000; Davies et al., 2002). Notably, if there is adequate sap flow through the roots, the ABA signal is

41   transmitted through the xylem to the leaf, as demonstrated by Dodd et al. (2008). According to Davies and Hartung (2004), it

42   is proposed that plants subjected to partial root-zone drying (PRD) demonstrate improved performance compared to plants

43   under deficit irrigation (DI) when an equal amount of water is applied. This is attributed to the ability of PRD to stimulate

44   root growth and maintain consistent signalling of abscisic acid (ABA) to regulate shoot physiology. Davies and Hartung

45   (2004) stated that the effects of PRD on plant growth, yielding and functioning are quantitatively different from those of

46   RDI. One of the advantages of PRD when operated properly, is that plants sustained and even increased shoot and fruit

47   turgor even though a reduced amount of water is applied to roots (Mingo et al., 2003). On the other hand, one of the

48   disadvantages of RDI is that the entire root zone is allowed to dry out, the roots can become stressed and damaged and if not

49   rewetted can die and signalling may diminish. Conversely Fernández et al. (2006) stated that not always a PRD treatment has

50   been found advantageous as compared to a companion regulated deficit irrigation (RDI) treatment and demonstrated it in a

51   study on olive trees in which sap flow measurements, which reflected water use throughout the irrigation period, showed no

52   evidence of stomatal conductance being more reduced in PRD than in RDI trees. Collins et al. (2009), in an experiment on

53   the grapevine (Vitis vinifera L.) show that the response to PRD applied at 100% ETc and deficit irrigation applied at 65%

54   ETc was the same, increasing stomatal sensitivity to vapour pressure deficit and decreasing sap flow. According to Cai et al.

55   (2022), while stomatal conductance is a significant aboveground hydraulic factor influencing water use in crops, it should

56   not discount the role of belowground hydraulics, as changes in soil-plant hydraulic conductance have been found to drive

57   stomatal closure (Abdalla et al., 2021). This highlights the crucial importance of studying electrical activity in the soil.

58   The plant's natural bioelectrical activity is necessary for its physiological processes. Plant scientists represent it by a water

59   column where the ions move from bottom to top and vice versa due to gradients of water potentials. In their studies, Voytek

60   et al. (2019) and Gibert et al. (2006) successfully linked the measurements of electrical potential in the ground and in the tree

61   stem to the RWU and sap flow respectively. The use of active methods such as electrical resistivity tomography (ERT)

62   allows for spatial and temporal analysis of the subsoil. Recent advances in electrical tomography imaging, in particular

63   reduced at the plant scale, show their effectiveness to measure changes in soil water content associated with the RWU (e.g.

64   Cassiani et al., 2015, 2016; Mary et al., 2018). Note that the correlation between root water uptake and soil water content

65   changes exists when averaged over a larger spatial scale than the scale at which soil moisture redistribution can compensate

66   for local root activity. The determination of these spatial scales depends on the soil hydraulic properties. This correlation

67   between root water uptake and changes in soil water content can also be influenced by the time scales in addition to spatial

68   scales. The ability to discriminate between them relies on factors such as the soil hydraulic properties, rates of local water

69   extraction, and the temporal dynamics of water redistribution in the soil (Anonymous Reviewer, 2023). Applications of

70   geoelectrical methods to evaluate water use efficiency are increasing. Recently in an experimental Citrus orchard, Consoli et

71   al., (2017), Vanella et al., 2018 and Mary et al., (2019a) showed that the observed drying pattern resulting from an elevated

72   evapotranspiration rate (ER) in the non-irrigated section of the root zone matches the root distribution in that area, while the

73   observed wetting pattern arising from a decreased ER in the irrigated section of the root zone can be attributed to the

74   irrigation itself.

75   However, processes occurring in the rhizosphere can affect the soil ER in various ways. Roots induce changes in the soil

76   structure in terms of porosity and hydraulic conductivity which ultimately modify the water pathways and fluxes and thus the

77   ER itself. Soil structure changes may have a relatively smaller effect on ER than root water uptake RWU, although this may

78   differ for species with extensive root systems like woody species; this is further true during rainfall or irrigation considering

79   water redistribution and channelling influenced by varying root anatomies and causing dynamic variations in ER. Stemflow

80   channelling by roots is an example of how water from rain or irrigation can be driven to soil recharge by the root structure.

81   Conversely, root uplift in agroforestry shows how water can move from the deeper layers to the top via the roots. Roots also

82   affect the soil ER through the geochemical changes associated with root exudates and root symbiosis. At the interface

83   between soil and roots, the chemical gradients and concentrations can drastically differ from those observed in the soil

84   regions not affected by the roots. Although this can have a significant impact and be a valuable source of information, only a

85   few studies have extended the ERT and the induced polarisation (IP) to observe these changes (Weigand, 2017; Weigand

86   and Kemna, 2019; Tsukanov and Schwartz, 2020, 2021). As of today, the electrical behaviour of individual roots remains

87   poorly understood, particularly with regard to their changes in type (from hair roots to fully lignified roots), space, time, and

88   whether the root is active or not (Ehosioke et al., 2020).

89   The geophysical approach extends the scope of traditional methods to evaluate soil water content (SWC) using time-domain

90   reflectometry (TDR) sensors and the calculation of RWU (Jackisch et al., 2020). In the field, the spatial resolution is

91   controlled (in ERT or IP) by the arrangement of the electrodes and acquisition parameters (Uhlemann et al., 2018), while the

92   temporal resolution is controlled by the time it takes to complete a full sequence measurement.

93   Rhizotrons are one of the earliest and most effective tools for studying root growth and functioning, both in the field and in

94   the laboratory (Taylor et al., 1990). They are transparent boxes that allow the direct observation of the roots during plant

95   growth and changes in soil conditions. Rhizotrons also provide valuable support in multidisciplinary studies, allowing other

96   methods to be more easily and precisely deployed, so that their results more reliably interpreted. For example, a load scale is

97   often mounted in combination with the rhizotron in order to weigh the system, which allows inferring the quantity of water

98   lost by the plant over time. This set-up is inspired by the lysimeter and is widely adopted to measure the water balance of the

99   soil-plant interactions. For example, in a rhizotron, Doussan and Garrigues (2019) use the light transmission 2D technique

100   to infer root water uptake with respect to their genotypes.

101   The very few studies conducting geophysical tomography imaging in the laboratory using a rhizotron proved a certain

102   efficiency in studying the interaction between soil physics and plant physiology for predicting plant response to

103   environmental stresses (Weigand, 2017, 2019; Peruzzo et al., 2020). It allows for high-resolution tomography by reducing

104   the size, diameter, and spacing of the electrodes. The entire soil profile is easily accessible by placing electrodes on the side

105   of the rhizotron, easing the depth resolution limitation inherent to surface-based geophysical methods usually used for field

106   acquisition.

107   Although there is a good momentum for the use of geophysical methods applied to agronomy (Garré et al., 2021), a number

108   of gaps still need to be addressed. All the indirect root effects on the soil ER affect the evaluation of the soil water content,

109   making the interpretation of ERT to quantify RWU sometimes difficult (Ehosioke et al., 2020).

1.1.   Current pathways in roots under water stress constraints

111   Current pathways in roots remain certainly the main unknown since there is a gap in techniques to measure

112   it non-destructively (Ehosioke et al., 2020; Liu et al., 2021). The current pathways in roots are possibly

113   linked to RWU. Lovisolo et al. (2016) describe in detail the flow of water from root water uptake and the

114   processes occurring at the cell scale. In any case, root water uptake is not distributed equally over the

115   whole root system, in part, due to heterogeneous soil conditions. For the same reason as soil saturation can

116   change over time, RWU is also varying in the time. The concept of active roots has been previously

117   employed by several authors (Frensch and Steudle, 1989; Doussan et al., 1998; Garrigues et al., 2006;

118   Srayeddin and Doussan, 2009) to characterise the spatial variability of root water uptake. In this context,

119   plants adapt by reducing radial conductivity in dry regions, enabling them to redirect their uptake towards

120   wetter areas with higher soil conductivity. This mechanism allows plants to maintain a consistent rate of

121   water uptake while sustaining higher plant water potentials. For active roots, root water uptake consists in

122   a moving water from the root tip (which is usually much more electrically conductive due to high water

conductivity at its proximity) in the radial direction via cellular (symplastic way) and between cells (apoplastic way) until it reaches the xylem which transport it in the axial direction towards the upper part. Water flow can encounter resistances due to suberization (conversion of the cell walls into cork tissue by development of suberin), which is naturally driven as a consequence of root growth (secondary roots are more suberised than primary roots) but it can also be the consequence of plant stress (Malavasi et al., 2016; Song et al., 2019). The process can cause reductions in water conductivity through the root system by limiting the permeability of the root tissue, thus leading to changes in the plant's ability to take up water. Aroca et al. (2012) describes in a generic manner the plant responses to drought stress.For the specific PRD case, there is a complex tradeoff induced by root suberization between reducing radial flow (as a consequence of ABA signalling sent by the roots) to conserve water in the soil but keeping the axial flow active.   This can be done for instance by adjusting the xylem vessels size and quantities. Although suberisation is usually a long-term process, studies show that PRD can promote and accelerate the process of suberization in response to water limitation. Finally during PRD conditions we can also observe transfer of water from the wet to the dry side through the roots (overnight) in a process called redistribution (Yan et al., 2020), which induces spatio-temporal variations in RWU that ultimately also influences electrical current pathways in roots.

A direct approach to analysing the active part of the root system consists of an injection of current stimuli into the plant stem. There is a variety of stem based methods used in the literature with applications ranging from biomass estimation, root morphology to root physiology (root activity). At a single frequency, we distinguish between ECM methods which rely on capacitance measurements and are commonly used to study root systems at the plant scale and EIM, which measures both capacitance and resistance. Capacitance represents the polarization processes and measures the charges stored during the current flow. Both use the fact that the root can polarise at the soil-root interface and inside the root to infer direct root-related information such as dry and wet mass, surface area,...). A second group of methods Electrode Impedance Spectroscopy (EIS) uses a range of frequencies to capture the polarisation processes

148   sensitive to the root physiology and anatomy. For a detailed description of the methods, the reader is

149   invited to refer to (Ehosioke et al., 2020). The stem based approach has been developed for years by plant

150   physiologists, starting from the theory developed by Dalton (1995) who conceptualized the current

151   pathways through the root xylem by an equivalent parallel resistance-capacitance circuit. The theory holds

152   under the assumption that the current flows throughout the most conductive path and is held (thus inducing

153   polarization) by the root cell membranes before being released into the soil. Fine root connections and

154   mycorrhiza facilitate the efficient transfer of injected current into the soil at contact points between roots

155   and the soil, resulting in a distribution of current sources within the ground. Contrasting experimental

156   results have challenged the relationship between root electrical capacitance and root traits in different

157   crops, with studies highlighting the potential contribution of the stem, rather than the roots, to the overall

158   measured root electrical capacitance and the occurrence of current leakage at the proximal part (Urban et

159   al., 2011; Dietrich et al., 2018; Peruzzo et al., 2020).

160   Without being able yet to give hints about the electrical current pathway, recent advancements in the

161   development of explicit RWU models, based on plant hydraulics, provide insights into how robust

162   capacitance models hold and under which conditions. We learnt, for instance, that at the root level, RWU

163   models account for the anisotropy by separating the root hydraulic conductance into two terms i.e. axial

164   and radial (Javaux et al., 2008; Couvreur et al., 2012). Figure 1 draws inspiration from the electrical circuit

165   analogy of RWU (Root Water Uptake) proposed in previous works (Doussan et al., 1999, Manoli et al.,

166   2014 and Couvreur et al., 2012 and Cai et al., 2022). ~~According to Fig.1~~In dry soil conditions, the

167   primary part of the potential drop happens within the soil-to-root connection, while in wet soil conditions,

168   the main portion of the potential drop is in the plant section. **~~I~~in dry soil, the gradient $\Delta\psi_{soil} = (\psi_{soil} - \psi_{soil\text{-}root})$**

169   **is higher than in wet soil. As the soil conductance ~~gs~~ g_s is linked by the relationship between the**

170   **transpiration rate over the $\Delta\psi_{soil}$, for the same evaporation rate, g_s is ~~increasing~~decreasing when the**

171   **soil dries out. ~~For a constant soil conductance, when the evaporation rate is increasing the gs increase. The~~**

172   **~~same occurs for the root conductance g_r.~~ The root axial water flow rates Qx (~~L3T−1~~L^3T^{-1}) and root**

173   **radial water flow rates Qr (L^3T^{-1}) can be solved analytically by solving the system of equations of**

174   **Ohm's and Kirchhoff's laws (Couvreur et al., 2012)**.

175

176

177   The same applies to the stem-based methods as root hydraulic conductance and electrical conductivity are

178   likely to vary conjointly. Up to now the relationship between root water content and root hydraulic

179   conductivity with ERhas not been firmly established. Many other parameters such as root function, age,

180   water retention capacity and transpiration rate in particular can affect the water flow as well as the current

181   pathway of stem-based methods (Ehosioke et al., 2020).

182   Peruzzo et al. (2020) hypothesize that drought stress can also reduce electrical current leakage wherein the

183   current exiting the plant root at the proximal part is decreased, particularly for woody species.

184   Furthermore, as expected, the frequency of the injected current plays an important role in the capacitance

185   measured. At high frequencies, both the longitudinal conductivity and radial conductivity increase

186   (Mancuso 2012; Ehosioke et al. 2020), which can also cause current leakage problems (Gu et al., 2021).

187   The measure of plant responses over multiple frequencies, a method called Electrical Impedance

188   Spectroscopy (EIS) is more time-consuming but more informative since different polarisation processes

189   can manifest themselves in the signal (Ehosioke et al., 2020). The contrast of electrical resistivities

190   between soil and roots plays a fundamental role as reported e.g. by Cseresnyés et al. (2020). Gu et al.

191   (2021) stated that the potential to directly quantify root traits under dry conditions is higher than under wet

192   conditions and interpreted this as a result of the fact that the root electrical longitudinal conductivity is

193   higher than that of the soil under dry conditions. The instrumentation and acquisition schemes used for

194   impedance are also questionable and the optimal experimental setup of measurement remains to be

195   determined (Postic and Doussan, 2016). The number and the position of the stem and the return electrodes

196   are a cause of uncertainties (electrode contact resistance, etc.). Peruzzo et al. (2021), in a three channels

197   experiment, were able to provide direct access to the response of stem and soil, which ultimately allowed

198   the decoupling of the root response. Evidence showed the presence of current leakage in herbaceous root

199   systems, a significant contribution from plant stem, and a minor impact from the soil.

200   Gu et al. (2021) stated that in addition to the traditional regression model used for predicting root traits

201   using the impedance method, a forward model would help to illustrate the importance of these different

202   factors. In order to cope with the main drawbacks of the impedance methods, we propose the so-called

203   Electrical Current Imaging (ECI) method, a physically based approach based on recovering the current

204   density distribution instead of simply calculating the total resistance/capacitance. This method is also

205   referred to as mise-à-la-masse (MALM) in the applied geophysics literature. The current imaging methods

206   hold some promise to offer a first set of evidence about the current pathways: This is a popular technique

207   adopted e.g. by the neurosciences community, where the current density in the human brain correlates with

208   diverse patterns of neural activity (Kamarajan et al., 2015). Peruzzo et al. (2020) applied it for plant roots

209   imaging with relative success, as the authors stated that all the current leaks at the plant's proximal part i.e.

210   at the shallowest contact of the plant stem with the soil. For the ECI approach, the Poisson's equation

211   serves as a physical model for the electrical current flow. As current flow is modulated by the conductivity

212   of the soil, the ECI approach is always combined with ERT in order to recover of the soil resistivity

213   distribution.

214   **1.2.**   **Study aims and assumptions**

215

216   The aim of this study is twofold:

217   (i) we aim at showing the correlation between the current path through the root system and the active root

218   zones. This assumption is based on the notion that soil and root hydraulic conductances are positively

219   associated with electrical conductances.

220   (ii) we want to investigate how the soil water content affects the current path.

221   For this, we rely on the following assumptions:

222   - changes in soil water content measured by ERT are a relevant spatial proxy of root activity and can be

223   used as an indicator of the actual plant transpiration by correlating them with variations of the total

224   rhizotron measured weight.

225   - During the implementation of root-zone limited water availability, when a portion of the root system in

226   the dry zone becomes deactivated, injected current in the stem tends to preferentially propagate towards

227   the side where the root system is irrigated.

228

229 **2.**   **Material and methods**

230

231   **2.1.**   *Experimental setup*

232   **2.1.1.**   **Rhizotron**

233   The experiment was conducted using a rhizotron 50 cm wide, 50 cm high, and 3 cm thick, with a

234   transparent screening face. The front of the rhizotron was equipped with 64 stainless steel

235   electrodes with 4 mm diameter which did not extend into the rhizotron's inner volume (Fig. 1).

236   An additional line on the top surface of the rhizotron was composed of 8 electrodes inserted to 1

237   cm depth. A growth lamp was installed above the rhizotron and turned on during daylight hours

238   (from 7 am to 7 pm). The rhizotron was closed on all sides and watertight, with only 8 small holes

239   used for the irrigation at the surface and the central hole where the plant is placed. We considered

240   the surface of these holes to be sufficiently small to neglect the possible effect of evaporation

241   through them. An outlet point was placed on the bottom right side ($z=5$cm) and the rhizotron was

242   always saturated below this point. In the course of the experiment (after the growing period) no

243   water discharge was observed through the outlet point.

244

29
30
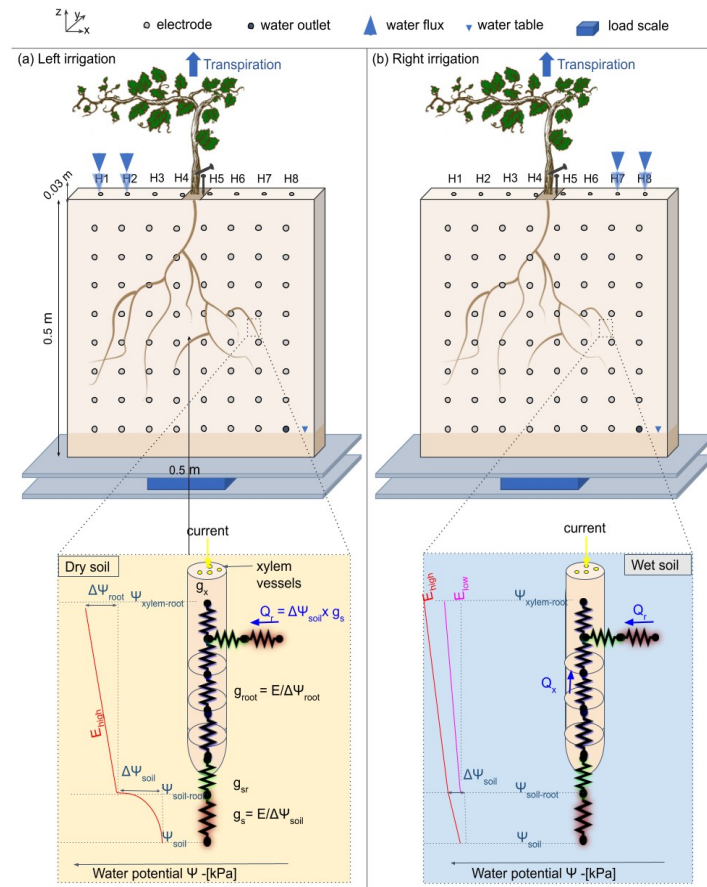
Figure 1: Conceptual figure showing the position of the plant in the rhizotron. The water input was done alternatively from left (a) to right (b) via small holes on the top of the rhizotron (H1 to H8). The roots are free to grow on both sides of the rhizotron. The circles on the screening face show the locations of the electrodes. Two additional electrodes (needles) are used for the ECI, one for the stem injection and the other for the control soil injection next to the stem. The rhizotron is weighted by a central point load scale (PC60-30KG-C3, Flintec) mounted between two support plates in plexiglass. The line below describes the state of the art of hydraulic conductivity at a single root and the distinction between dry (c) and wet (d) soil. The figure draws inspiration from the electrical circuit analogy of RWU (Root Water Uptake) proposed in previous works (Doussan et al., 1999, Manoli et al., 2014 and Couvreur et al., 2012 and Cai et al., 2022). In a recent article, Cai et al. (2022) schematized the gradient of potential ψ_{soil}, $\psi_{soil-root}$ and ψ_{root}, along with the corresponding hydraulic conductances of the soil, the soil-root interface, and the root (represented as g_s, g_{sr}, and g_r, respectively), in response to high or low transpiration demand (E). Note that the soil-root interface and the xylem cell interfaces are seats of current polarization due to the formation of the Electrical Double Layer (EDL) well described in Tsukanov and Schwartz (2021).

259   ### 2.1.2.   Plant treatment

260   At the initial stage of the experiment, we used a *Vitis Vinifera* cutting with a pre-developed root

261   system (rooted cutting var. Merlot) was used. The cutting was grown in hydroponic solution

262   (modified Hoagland medium) for 4 months before being transferred into the rhizotron. This was

263   followed by a growing period of 5 weeks with irrigation applied over the whole width of the

264   rhizotron every 3 days.   The vine was then irrigated with a nutrient solution (see Table 1)

265   following a PRD protocol.

266

267   ### 2.1.3.   Soil type

268   The experiment was conducted in a sand-peat mixture (50-50 m/m%). The applied sand was high-

269   purity quartz sand (SiO_2 = 99%) of grain size comprised between 0.1-0.6 mm and the peat was a

270   normal commercial acidic sphagnum peat. During the course of the experiment, the soil was

271   stable through time with very low compaction (1 cm) observed at the end of the experiment

272   (already observed by Doussan & Garrigues, (2019) for soil with a lower density than 1.5-1.6

273   g/cm^3). The sand-peat mixture was chosen as a compromise between water retention and

274   drainage. We estimated the porosity at the beginning of the experiment as equal to 55% using the

275   ratio of water weight after saturation to the total volume of the rhizotron.

276   ### 2.1.4.   Irrigation schedule

277   We controlled the water supply for each irrigation event based on the data obtained from the

278   scale, ensuring that the plant received 75% of the measured transpiration accumulated since the

279   last irrigation cycle. For each cycle, the wetting side changed (from left to right). Note that in this

280   experiment, we did not consider a physical barrier to separate the two sides of the rhizotrons to a

281   split-roots configuration as is the case for other PRD experiments conducted in the laboratory

282   (Martin-Vertedor and Dodd, 2011; Sartoni et al., 2015). In general, the use of physical barriers in

283   Partial Root Zone Drying (PRD) experiments is not always a standard aspect of the setup.

284   Table 1 describes all cycles conducted from May 13th to July 12th 2022:

285   -   The goal of Cycle number 0 was to ensure plant adaptation and growth after
286   transplantation.
287   -   Cycle numbers 1 to 3 aimed at starting the PRD irrigation with half of the rhizotron
288   volume irrigated; i.e. we irrigated the side through a total of four holes out of eight (see
289   Fig. 1).
290   -   From cycle number 4 to 10, we restricted the water input only to the two left/right most
291   holes.
292   -   Between cycles 4 and 5, we added intermediate irrigation on the full length of the
293   rhizotron.

294   For the irrigation, we used a nutrient solution (modified Hoagland) (Hoagland and Arnon, 1950)

295   having an electrical conductivity equal to 2470±5 μS/cm (at ~25°C), except for cycle 3 where tap

296   water was used (560 μS/cm).

297

~~Date~~Irrigation time (YYYY-mm-dd HH:MM)	Hole (H) location (c.f. Fig. 1)	Quantity (mL)*	Cycle nb
2022-05-13 16:25	All		0
2022-05-19 17:00	H1;H2;H3;H4	200	1
2022-05-25 14:30	H5;H6;H7;H8	260	2
2022-06-01 15:50	H1;H2;H3;H4	290	3
2022-06-08 11:50	*H7;H8*	*305*	*4*
2022-06-10	*All*	*60*	*- (~~3~~4bis)*
2022-06-15 17:25	**H1;H2**	**350**	**5**
2022-06-22 16:45	*H7;H8*	*375*	*6*
2022-06-29 13:45	**H1;H2**	**386**	**7**
2022-07-05 18:10	*H7;H8*	*431*	*8*
2022-07-11 13:15	**H1;H2**	**431**	**9**

298

299   **Table 1: Irrigation log, indicating the ~~date~~irrigation initial time, the location where the water was**

300   **input and the corresponding cycle number considered in the results. ~~Colors~~The font correspond to**

301   **the side used for the irrigation, ~~green~~bold is on the left side while ~~orange~~italic is on the right side. ***

302   **Quantity in total distributed over all the holes.**

303   **2.2.   Electrical Resistivity Tomography**

304   Electrical Resistivity Tomography consists in reconstructing the subsoil ER using an array of electrodes

305   (Binley and Slater, 2020). In this study, a total of 72 stainless steel electrodes were used, 64 electrodes

306   formed a grid, 5 cm spaced, covering the screening face of the rhizotron, and an additional line of 8

307   electrodes was posed at the top surface. Electrodes are needles 4 mm in diameter and 80 mm in length, but

308   only their tip is in contact with the soil. ERT involves the measurement of transfer resistances following a

309   sequence describing a combination of varying injections (AB) and potential (MN) pairs of the electrodes.

310   We used a custom sequence composed of 4968 quadrupoles including the reciprocals (e.g. Parsekian et al.,

311   2017), and the measurement were conducted using a Syscal Pro (Iris Instrument) resistivity meter., The

312   sequence was optimized over the ten physical channels of the instrument in order to reduce the acquisition

313   time to approximately 30 min. The data acquisition parameters were constant along the monitoring, with a

314   minimum required V_p of 50 mV, a maximum injection voltage V_{AB} of 50 V, and a number of 3-6 stacks

315   with the on-time fixed to 250 ms each.

316   **2.3.   Electrical Current Imaging**

317   The electrical current imaging (or Mise-à-la-masse) method was logistically similar to ERT. The sequence

318   nevertheless varies, as the pairs of injection electrodes were kept constant with the positive pole (+I)

319   electrode located on the stem, and the return (-I) electrode located in the bottom right of the rhizotron. The

320   potential electrodes pairs (MN) vary according to a custom sequence. For the stem current stimulation, we

321   inserted a small stainless steel needle (2 cm, 1 mm diameter) into the plant stem at 5 cm from the grafted

322   point. The needle was inserted all the way to the centre of the stem (Fig. 1). Before each measurement, we

323   added a few drops of water to the stem needle in order to reduce the stem contact resistance (to values

324   between 41 and 66 kΩ). The current was guided to the root system via the stem and then released into the

325   soil.

326   As the effect of the stem contact resistance affects the measured voltage, a control soil injection was

327   systematically made. In that case, the current was injected into the soil close to the plant (Fig. 1). A

328   qualitative comparison between the control soil injection and the stem injection plant could be made to

329   discriminate the effect of roots. Furthermore, soil control injection served as a visual calibration for the

330   inversion of the current source knowing that the injection is punctual and occurs at a known position.

331

332   **2.4.**   **Weight monitoring for the estimation of transpiration**

333   In order to track the weight changes due to the transpiration of the plant, the rhizotron was equipped with a

334   single point load cell (PC60-30KG-C3, Flintec), mounted between two plates in plexiglass supporting the

335   rhizotron (Fig. 1). The data were logged with a sampling rate of 5 min using the weight indicator DAD-

336   141.1. The total weight of the rhizotron is about 20 kg and the expected resolution according to the sensor

337   datasheet is 0.1 g. The variation due to temperature was monitored, on average in May at 22°C, and in July

338   at 25°C. To avoid sharp signal perturbation, during the irrigation and the acquisition of geophysical data

339   the logger was paused.

340   **2.5.**   **Leaf gas exchange observations**

341   In order to monitor the physiological response of the plant during the course of the experiment, stomatal

342   conductance to water (g_{sw} [mmol H_2O m^{-2} s^{-1}]) measurements were performed on vine leaves with an open

343   flow-through differential porometer (LI-600, Li-Cor Inc., Lincoln, Nebraska, USA). The stomatal

344   conductance is a measure of the density, size, and degree of opening of the stomata, therefore it can be

345   used as an indicator of plant water status (Gimenez et al., 2005). The measurements were carried out on 26

346   leaves in the morning hours (at 10 a.m.), once (on 8th June 2022) just before irrigation (severe water

347   stress), and once (on June 16, 2022) one day after irrigation (mild to low water stress). For the tracking of

348   the plant development, the length (L) and the width (W) of every leaf were measured every 2 weeks from

349   the beginning of the growing period until the end of the experiment. From this data the total leaf area (LA)

350   was estimated according to three models: LA1 = 0.587 (L×W) (Tsialtas et al., 2008); LA2 = -3.01 + 0.85

351   (L×W) (Elsner and Jubb, 1988); LA3 = -1.41 + 0.527W^2 + 0.254L^2 (Elsner and Jubb, 1988).

2.6. Data processing

2.6.1. Analysis of ERT data

The ERT acquisition sequence was initially tested on the rhizotron filled with water of known conductivity and it offered good coverage on most of the rhizotron surface with a slight decrease on the sides. The soil electrode contact resistances varied over the course of the experiment between 5 and 20 kΩ. Data were filtered on the basis of the percentage of variations between direct and reciprocal measurements. We chose to eliminate the data with reciprocal relative errors larger than 5%, for all the time steps. The number of rejected data varies from 9% to 39 % of the total (see Table A1) with a median of 11%. Transfer resistances were inverted using the open-source code ResIPy (Blanchy et al., 2020) based on the Fortran R3t code (Binley, 2015). The inversion mesh is an unstructured grid composed of tetrahedra, created using Gmsh (Geuzaine and Remacle, 2009). Two distinct strategies can be used: (1) individual inversion which consists of building a model of resistivity at a given time, and (2) time-lapse inversion (difference inversion) where the difference in resistivity is inverted between a given survey and a background survey (in this case, the background survey is the previous one). In this study, we used the ~~second~~first approach, which allowed filtering of systematic noise and highlights variations (as a percentage of differences) between two times.

2.6.2. Analysis of current density

The mathematical formulation for the inversion of the current source density (CSD) has been developed in previous studies. It consists in searching for a linear combination of Ohm's law, for a series of current punctual sources (also called virtual sources) minimizing the misfit between simulated and observed data. The algorithm was initially tested on the rhizotron filled with water of known electrical conductivity and a single isolated cable (see the procedure from Peruzzo et al., 2020). It is important to note that the CSD inversion relies on the knowledge of the medium conductivity (as in the Poisson's equation, the current is modulated by the electrical conductivity).

377   Thus, we used the inverted ER values as the resistivity distribution for the forward modelling in

378   the current density inversion. As for ERT, choices must be made on how data and models are

379   weighted and regularised during the inversion. In this study, we run unconstrained (no prior

380   information) inversions for all the time steps with a regularisation (smoothing using the first

381   derivative). The numerical routine includes a "pareto" functionality wherein regularization and

382   model-to-measurement fit are traded off to estimate the optimum regularization weight wr. The

383   code used for this inversion is available at https://github.com/Peruz/icsd.

384   **2.6.3.   Calibration of petrophysical relationships**

385   In order to estimate the soil water content in the rhizotron during the experiment, we needed to

386   adopt a suitable constitutive model, starting from the available ER measurements.

387   Archie's (1942) law (eq. 1) is a widely used empirical relationship that relates the ER (ρ) of a bulk

388   material to its porosity (Φ), the contained fluid (water) electrical resistivity (ρ_{fl}) and the fluid

389   saturation (S). Archie's parameters a, m, and n are empirically derived, generally named as

390   follows: a is the tortuosity factor, m is the cementation exponent and n is the saturation

391   exponent.

$$\rho = a\rho_{fl}\phi^{-m}S^{-n} \tag{1}$$

392   We calibrated these parameters experimentally, as usually done, by collecting water saturation-

393   ER values over different soil samples. The sample holder (a cylinder of 150 mm inner height and

394   41 mm inner diameter) allows for a four-point measurement of the ER converted to apparent ER

395   using the appropriate geometrical factor. The adopted water electrical conductivity is known and

396   fixed (594 μS/cm at ~25°C). The rhizotron soil mixture pPorosity was assumed to be equal to

397   0.55, ~~which is the same of the soil mixture~~in the rhizotron. The sample was initially saturated to

398   field capacity and progressively desaturated. The field capacity was estimated by gravimetric

399   method approximately at 40% of volumetric water content (m^3/m^3). In total, 6 measurements were

400   collected at respectively 40, 33.6, 29.7, 28.2, 25.2, 22.4% of volumetric water content (m^3/m^3).

401   The obtained data are fitted with a least square optimization (using the Scipy library by Virtanen

402   et al., 2020). Here we assume a equal to 1 (consistent with the theoretical value), while the

403   exponents m and n are bounded during the optimization process to respectively [1.3-2.5] and [1 -

404   3]. With a coefficient of determination R^2 of 0.97 (figure not shown), we obtained values of 1.9

405   and 1.2 respectively for m and n.

406 ## 3.   Results

407   ### 3.1.   Physiological response

408   Photographs of the plant at the beginning and at the end of the experiment show the increment of leaf area

409   extension of the ~~upper part~~aerial part. The weekly measurements show a linear trend with time of the

410   estimated total LA (cm^2) whichever the model used (Fig. 2). At the end of the experiment water stress

411   symptoms werevisible on some leaves.

412   As for the root system, the depth variations could not be precisely assessed during the course of the

413   experiment. We observed that: (i) roots reached the bottom part of the rhizotron; (ii) spread all over the

414   rhizotron with a network of primary, secondary, and root hairs without any given architecture (some roots

415   grew vertically, others in diagonals); (iii) the roots kept a white appearance with apparently no lignification

416   even for the largest roots (>=3mm).

417
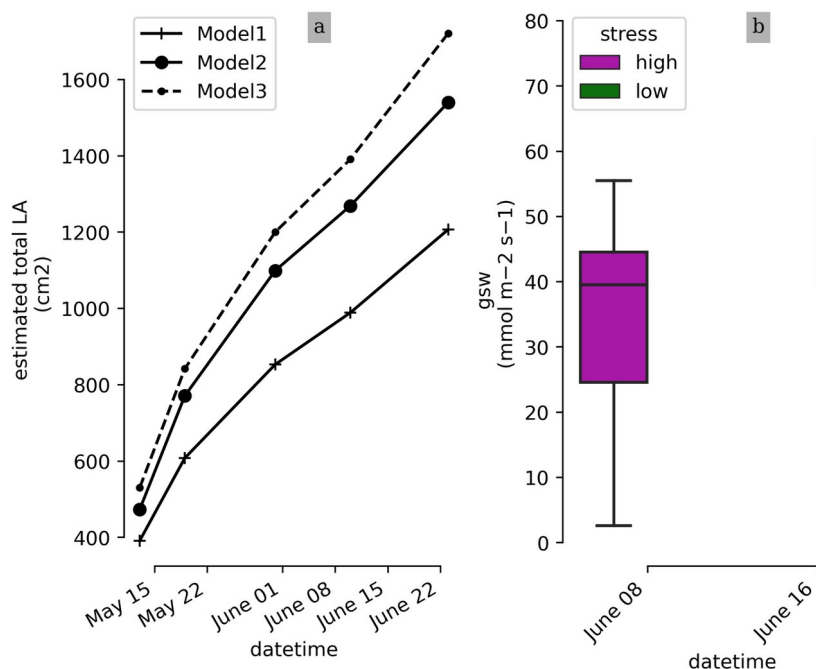
418
419 **Figure 2: (a) Time evolution of the estimated total leaf surface area (LA) for three different model estimators. (b) leaf stomatal**
420 **conductance (High and low stress distributions are significantly different with a T-test p-value = 4.3.10^{-3})**

421

422   The measurements shown come from the 26 leaves (c.f section 2.5) and indicate that the plant is under

423   high water stress at the end of the irrigation cycle (one week after the last partial irrigation, on June

424   8,2022), and under lower water stress one day after irrigation (on June 16, 2022). The mean, min, and max

425   values of the stomatal conductance (*gsw*) values are 37.8; 23.3; 55.5 mmol m^{-2} s^{-1} before irrigation,

426   respectively, and 50.6; 18.9; 78.1 mmol m^{-2} s^{-1} after irrigation, respectively. The result of the T-test shows

427   that their mean values are significantly different (p-value = 4.3.10^{-3}).

428

429   **3.2.   Transpiration rate**

430   No pre-processing of the raw data is needed for their interpretation. Fig.3 shows that, on average, during a

431   PRD cycle (about one week), 0.5 kg of water transpired. Also, the weight data show that the total weight is

432   decreasing from one cycle to the next, as expected, due to the PRD protocol. Although the total water

56
57

433   content is decreasing, the transpiration rate (slope of the weight variations) remains constant for each

434   cycle. At the very end of the experiment from July 9, an inflexion point is observed and the weight stops

435   decreasing. Zooming on a shorter time window, the variation of the raw data weight clearly shows

436   day/night patterns triggered by the hours when the light is switched on/off. On average, the water lost

437   during the day is nearly 20 times more than during the night (0.09 kg/day against 0.005 kg/night). Note

438   that there is no distinction between the hours of the day (due to artificial lighting).

439

440

441
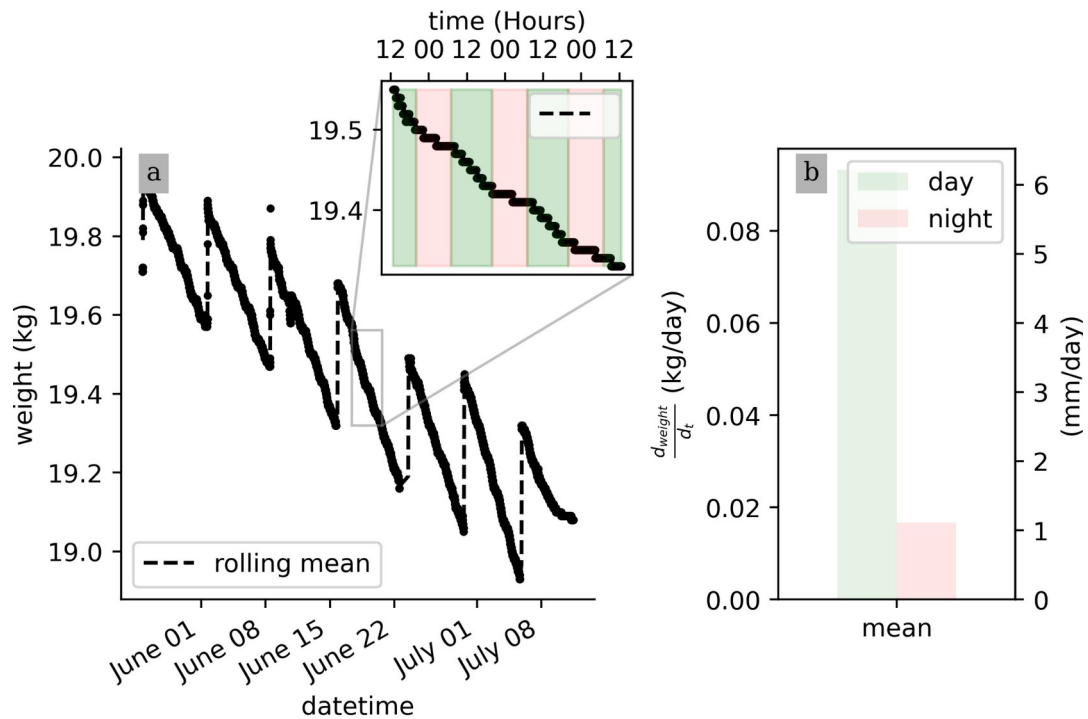
442
443   **Figure 3: Raw scale data collected over the course of the experiment (a) and a zoom on the week of June 20 to 25, where day and**
444   **night periods are respectively highlighted by the green and red shaded areas. (b) Calculated daily mean transpiration (d_{weight}/d_t)**
445   **during the day (green) and night (pink) periods.**

446

447   **3.3.   Time-lapse ERT**

448   In general, the ERT data quality is very good with a small percentage of total measurements exceeding a

449   reciprocal noise level of 5% (see Fig. A1 to A11) and with each inversion resolved within 2/3 iterations.

450   Figure 4 shows the trend for the PRD cycles (from cycles 0 to 9) for the mean average electrical

451   conductivity (in mS/m) for both the wet and dry sides of the rhizotron, taken as an average of each half of

452   the ERT inversion mesh elements. When PRD is applied over only two holes (from cycle 34) the irrigated

453   side shows a clear increase in electrical conductivity. To a much lower degree, the dry side is also affected

454   by the water input, likely due to water redistribution during drainage. When available, the temporal

455   dynamics between two irrigations show that the conductivity is decreasing rapidly on the irrigated side

456   during the 2 first consecutive days and more slowly afterwards (cycles C5/6 and C7/8 respectively; Fig. 4c

457   and Fig. 4d). As some water infiltrates also on the dry side, we also observe an increase in conductivity in

458   it. At the end of each cycle (the cycle length is about 7 days), the rhizotron returns to the equilibrium

459   condition, with a more homogeneous and stable average conductivity equal to 30 mS/m (mean of the dry

460   and wet sides). This is generally true for all times, except at the end of the experiment, cycles 7 and 8,

461   when the two sides are in different conditions.

462

463

464
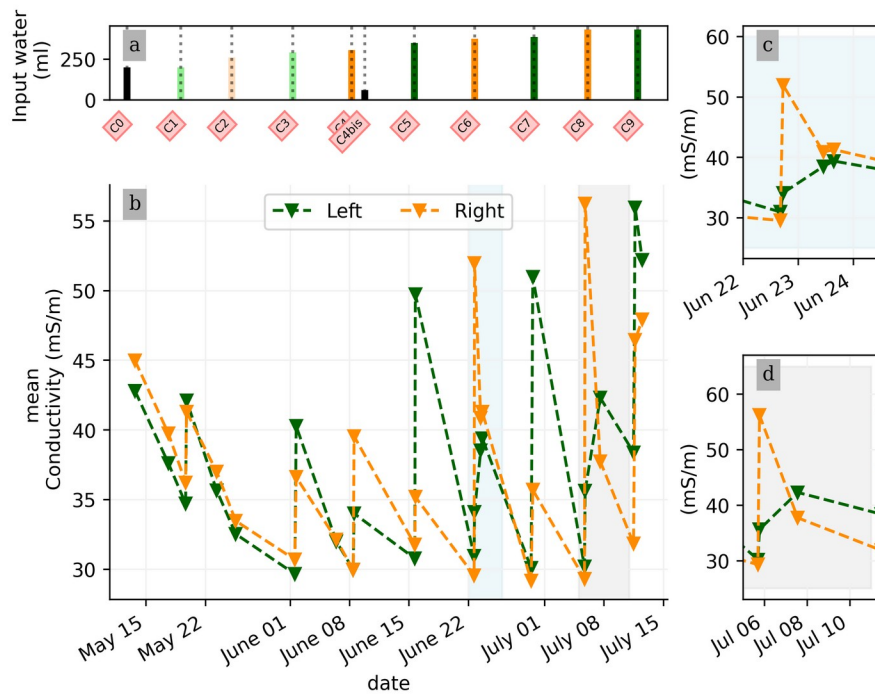
Figure 4: (a) Evolution of the quantity (in ml) of water input, spatially distributed with alternating between left (green) and right (orange) before and during the PRD irrigation. (b) Evolution of the mean conductivity (mS/m) average on each side, markers show the acquisition time. (c) and (d) are inset zooms showing changes before and just after the irrigation event.

We selected a time window between 29 June and 5 July showing the spatial variations of the ER before and after an irrigation event (Fig. 5). The application of background constraint inversion, as illustrated in Figure 5bc, leads to an interpretation suggesting that the blue regions correspond to areas where the soil is wet, whereas the red regions correspond to areas where the soil is drying. Before the irrigation, the top and left-most and right-most boundaries of the rhizotron exhibit higher ER (50 Ohm.m) than the central part (25 Ohm.m). One hour afterwards (+ 1H) the ER of the left irrigated side had dropped by 20% (estimated from the averaged values spanning from the middle of the rhizotron to the left boundary) .

All time-lapse inversions before/after irrigation are shown in Appendix A, including before the PRD. They all show that a decrease in ER is associated with irrigation patterns while an increase in ER has a

480   more complex spatio-temporal dynamics, not systematically associated with irrigation patterns. Positive

481   alterations in resistivity observed immediately after the irrigation event may potentially be artifacts

482   stemming from strong gradient in resistivity induced by the irrigation. Changes in ER after six days (day

483   +6) show that RWU effects are not limited to the irrigated part since the increase of resistivity was also

484   observed on the dry part. We Nnoteiced from a visual inspection of the rhizotron that a water table forms

485   at 0.4 m where the soil is saturated. This saturated zone level is not affected by the irrigation as no

486   increase after irrigation, and no decrease by the end of the irrigation cycles are visible. We assume that

487   most of the water fluxes were connected to the unsaturated part.
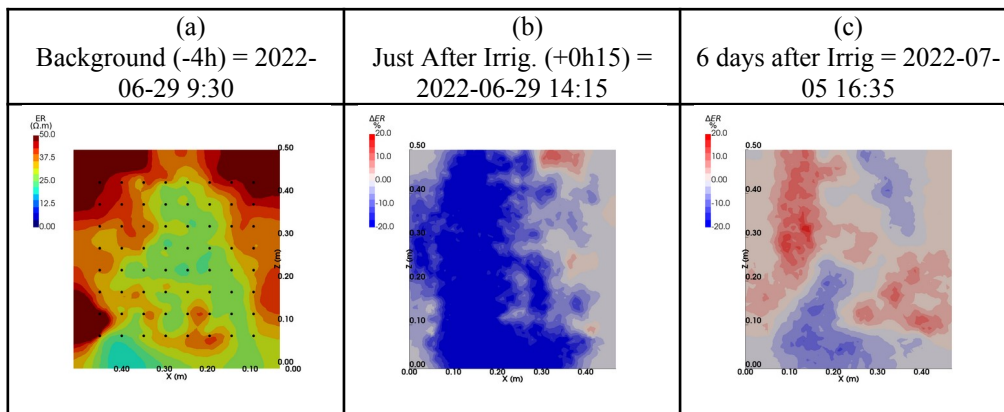
488

490 Figure 5: Spatial distribution of the resistivity (in **Ωm**) and changes (in %) in ER obtained by a time-lapse inversion between cycle
491 6 and 7 following partial left irrigation of the rhizotron. Time steps correspond to measurements before (a), 15 minutes (b) and 6
492 days (c) after irrigation started.

493

494   **3.4.   Time-lapse ECI**

495

496   Figure 6 shows the trend of the horizontal location (x coordinate) of the centre of mass of current density

497   during the PRD cycles (from −10 to 89), after the alternative wetting events on the left and right sides of

498   the rhizotron. Considering the modulation of current by soil electrical resistivity (ER), any bias in ER

499   could introduce errors in forward current source imaging and, consequently, affect the positioning of the
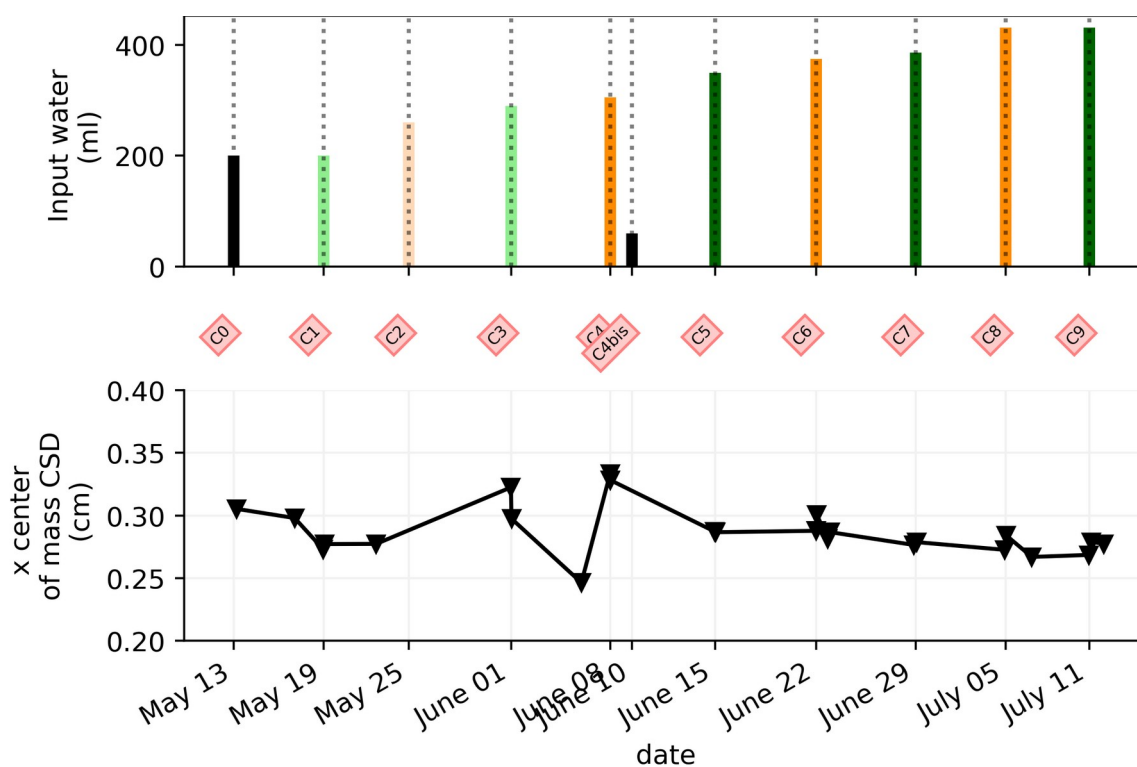
500   current source. The~~The soil CSD~~center of mass of the soil CSD is not shown as it is always pinpointed to

501   the location of the injection electrode whatever the irrigation pattern, as expected (Figure 7abc). This result

502   confirms the quality of the estimated ER background values used for the ECI forward model. For the stem

503   injection, the centre of mass of the current source density is distributed equally from left to right except for

504   cycle 4 when most of the current is located on the left (see Fig. B1 to B4). Conversely to ER variations, the

505   irrigation pattern does not significantly affect the current density distribution. The same applies to the

506   temporal dynamics between two irrigations where the current density centre of mass is stable and

507   distributed equally on both sides, as shown in Fig. 7. All the time-lapse inversion results of current density

508   for the soil and the stem injection are shown in Appendix B.

509

511 **Figure 6: (a) Evolution of the quantity (in mL) of water input spatially distributed alternatively between left (green) and right**
512 **(orange) during the PRD irrigation. (b) Evolution of the centre of mass (in the x direction) of the current density, while cross**
513 **markers show the acquisition times. Cycle ~~7 and 8~~6 to 7 windows were selected for the MALM time-lapse spatial analysis (Figure**
514 **7).**

515

Background = 2022-06-29 (cycle 76)	**Just after irrigation (H+1) = 2022-06-29 14:15**	**Day + 6 = 2022-07-05 16:35**
a (soil control, 10:24)	b (soil control, 15:02)	c (soil control, 17:55)

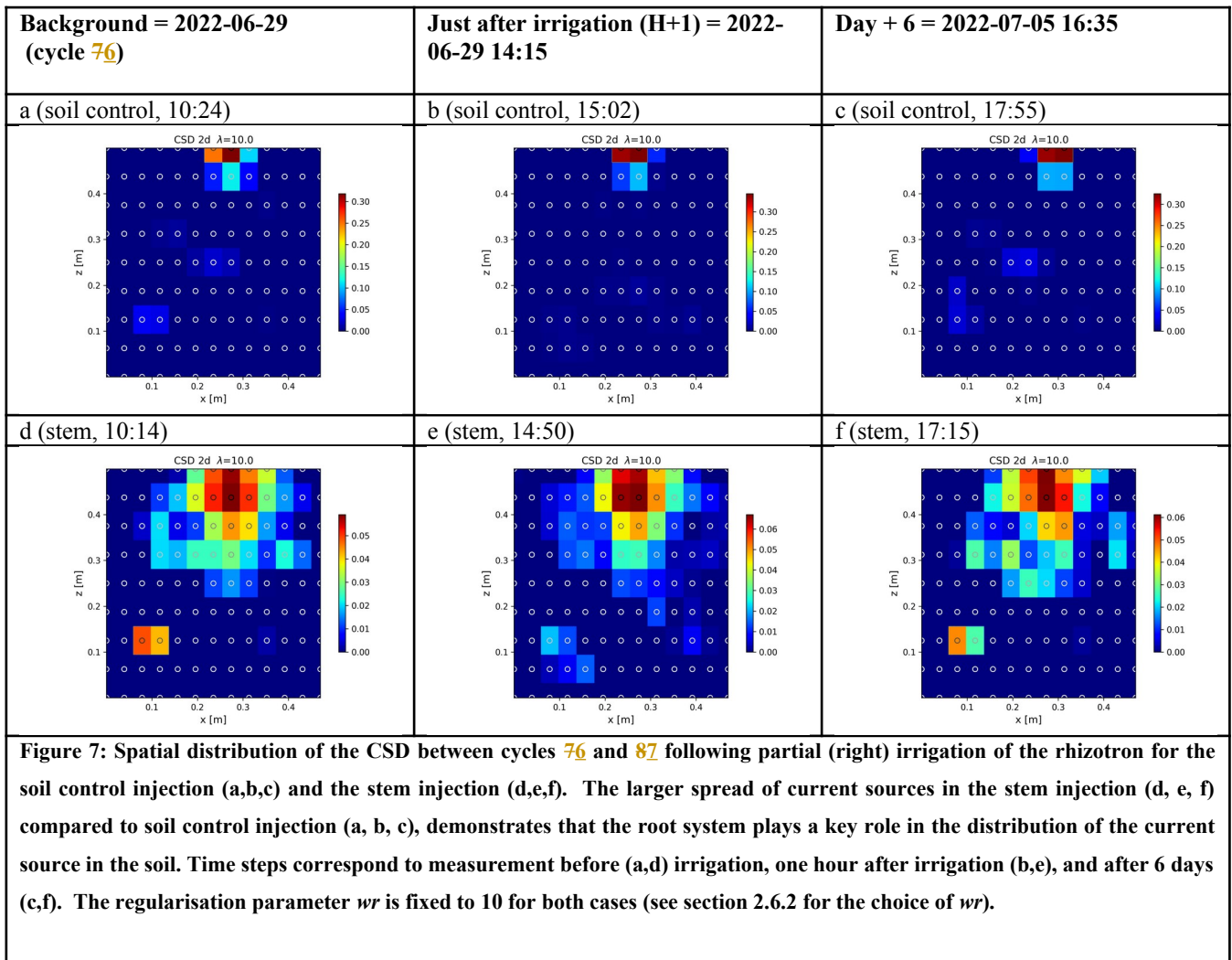| d (stem, 10:14)	e (stem, 14:50)	f (stem, 17:15)

Figure 7: Spatial distribution of the CSD between cycles 76 and 87 following partial (right) irrigation of the rhizotron for the soil control injection (a,b,c) and the stem injection (d,e,f). The larger spread of current sources in the stem injection (d, e, f) compared to soil control injection (a, b, c), demonstrates that the root system plays a key role in the distribution of the current source in the soil. Time steps correspond to measurement before (a,d) irrigation, one hour after irrigation (b,e), and after 6 days (c,f). The regularisation parameter *wr* is fixed to 10 for both cases (see section 2.6.2 for the choice of *wr*).

3.5. Correlations between soil parameters and estimated transpiration rates.

This section aims at drawing correlations between the soil parameters (ER, SWC, and CSD) and the transpiration estimated from the rhizotron weight data. We do not account for the weight variations due to the plant and root growth material (as this can be considered negligible relative to water dynamics). For each node of the mesh, ER values are translated to SWC using Archie's law with the calibrated parameters m and n (see Sect. 2.6.3). Averaging is performed on the mesh nodes falling within each side, with the middle point being defined as half of the rhizotron width, equivalent to 0.25m. To simplify, we assume that

525   both porosity and fluid water conductivity are homogeneous in space and time (i.e no mixing between the

526   tap water used for cycle 3 and the nutrient solution for all the other times). The maximum SWC observed

527   after irrigation is about 0.42 m^3/m^3 (figure not shown). The minimum SWC of about 0.25 m^3/m^3 is

528   repeatedly observed (see Fig. C1) just before each irrigation, meaning that the driest times are below field

529   capacity conditions (estimated at 0.4 m^3/m^3). By examining the fluctuations in weight, one can calculate

530   the corresponding changes in spatially averaged water content. Figure 8a illustrates a linear trend (R2=0.83

531   and p=2.96e-6) between the inferred water content variations from the scale and those obtained from ERT

532   (after Archie transformation). The most significant ~~negative~~positive changes in averaged water content are

533   attributable to the triggered irrigation, leading to a ΔΘ (change in water content) of -0.1. Conversely,

534   ~~positive~~negative changes primarily result from transpiration, with a maximum value located at +0.1.

535
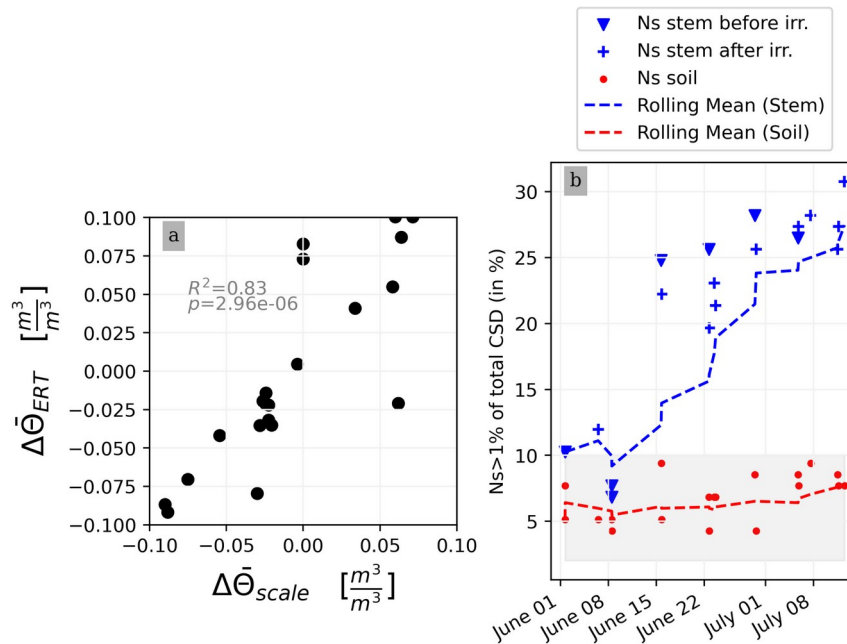
536 **Figure 8: (a) Changes in water content calculated from weight changes related to the changes in water content calculated from the**
537 **ERT measurements. (b) relationship between the number of the current sources (Ns) carrying at least 1% of the total density**
538 **(A.m-2) with respect to the time of the experiment. CSD results are obtained after inversion with a regularisation parameter wr of**
539 **10. Cases of the stem before cycle 3 (grey), after cycle 3 (black) and the soil (blue) injections. All cycles are considered.**
540
541

542

543

544   Figure 8b shows the relationship between the variation of the percentage of the current sources carrying at

545   least 1% of the total density (Ns1) used as an estimator for current density dispersion with respect to the

546   datetime of the experiment. For the soil injection (red dots), Ns1 is relatively constant between 5 to 10% of

547   the total number of possible injection nodes (grey area). For the stem injections, Ns1 increases over the

548   course of the experiment. From June 1st to July 8th, the Ns1 triple. The is no distinction between Ns1

549   measured before (triangle point) and after (crossed points) irrigation.

550 **4.   Discussion**

551   **4.1.   Validity of ERT and ECI in demonstrating the effects of the alternating irrigation scheme**

552   Our first assumption was that the variations in ER (or in SWC inferred from the ER) are relevant as a

553   proxy of root activity. Its validity has been checked against direct observation using the variations of

554   weights measured from the scale data used as an indicator of plant transpiration. On average, in our

555   experiment, the plant maintained high rates of transpiration to about 6 mm/day for each cycle except for

556   the last cycle (number 9) where a decline was observed (Fig. 3). This range is in line with another

557   rhizotron experiment where narrow-leaf lupin plants were grown: Garrigues et al. (2006) measured a mean

558   rate of 3 mm/day. It is commonly found in the scientific literature that changes in ER are associated with

559   root activity (e.g., Michot et al.,2003; Garré et al., 2011; Cassiani et al., 2015; Whalley et al., 2017). Here

560   we had further confirmation of this, with a significant correlation between ER changes and gravimetric soil

561   moisture changes (derived from the load cell) (Fig. 8). The leaf stomatal conductance and visual

562   observation of plant above- and below-ground material growth were additional ancillary data to interpret

563   the general state of the plant. Our observation is in line with the literature i.e. in general, low soil water

564   content (SWC) can lead to drought stress in plants, which can result in decreased leaf stomatal

565   conductance and less transpiration, and vice-versa.

566   A second assumption was that, when applying the alternative irrigation scheme, only one part of the root

567   system would be active and the current injected in the stem would only spread to the side where the root

568   system is irrigated. This assumption was not directly supported by the observations. Figures 6 and 7 show

569   that the influence of the irrigation pattern was negligible on the spatial distribution of the inverted CSD and

570   that the current distribution was not correlated with ER variations. It is true that active roots have higher

571   hydraulic conductivity but on the other hand, increased membrane permeability may encourages current

572   leakage into the soil. We nevertheless noticed that the CSD spatial distribution, while the rhizotron is

573   irrigated at its full length (cycles 0 to 3), was significantly different from the side irrigation cycles (Fig.

574   B4). Indeed, homogeneous irrigation without applying stress to the plant results in a very shallow current

575   leakage. Our observations potentially suggest that under conditions where soil electrical conductances are

576   high near the soil-root interface and even if there is good electrical contact between soil and roots, the

577   distribution of current source density might not be directly related to water uptake distributions. Further

578   research is needed to confirm this potential relationship.

579

580   **4.2.   Effect of soil water content and transpiration demand**

581   Soil water content can affect the distribution of the current leakage by influencing the minimum resistance

582   pathways, i.e., whether roots and/or soil provide the minimum resistance to the current flow. Literature

583   reports that electrical capacitance method better estimates crop root traits under dry conditions (Gu et al.,

584   2021). In order to make a comparison with capacitance studies, we assumed that if the current distribution

585   remains unchanged (i.e. leaking into the same areas), there must be minimal changes in the electrical

586   capacitance. In this study, supposing no impact of the initial model, Fig. 98 shows that there is no apparent

587   effect of the soil water content on the current density distribution. Note that the soil water content

588   estimated is the bulk contribution of roots and soil, as only one pedophysical relationship was used, while

589   recent studies tend to show that mixed soil-root pedophysical relationships are preferable (e.g. Rao et al.,

590   2018). Moreover, considering small-scale variations around individual root segments in terms of water

591   content and soil hydraulic properties becomes crucial for a comprehensive understanding of the system..

592   This is clearly limiting our ability to interpret the independent contribution of the soil and the roots, yet this

593   does not limit our ability to identify zones where water availability leads to root water uptake.

594

595   Based on Fig. 2 and 8b, the association between water stress and leaf development, along with

596   transpiration demand, is expected to be more prominent (and increasing during the course of the

597   experiment rather than the specific time points before and after irrigation). Indeed the fluctuations in water

598   content during various cycles, with or without stress, exhibited remarkable similarity. Both stressed and

599   non-stressed cycles experienced a drop in water content to similar low levels. Consequently, water content

600   does not appear to account for the variability in water stress. Instead, it is the increased transpiration

601   demand over time that seems to play a more significant role in driving the observed changes. At high

602   transpiration demand, stress may occur at higher soil water contents because the soil becomes limiting for

603   the root water uptake. The changes in water potential and water content in the vicinity of the soil-root

604   interface can potentially impact the electrical conductivity of the immediate soil surrounding the roots.

605   Consequently, as the experiment progressed, lower electrical conductances in the soil around the roots,

606   potentially led to a restriction in the flow of current between the root system and the soil. This, in turn, may

607   have resulted in a more uniform distribution of the electrical current source along the entire length of the

608   root system.

609
610

611   **4.3.**   **Possible mitigation of the PRD effect**

612   In general, a PRD irrigation experiment must comply with two criteria: (1) a minimum soil water content

613   to trigger a physiological response and, (2) a distinction between a wet and a dry side (Stoll, 2000). In our

614   experiment, the first criterion was met, but not the second. This provides an interesting piece of evidence,

615   leading to the following considerations:.

(1) According to McAdam et al. (2016) and Collins et al. (2009), ABA is triggered even by mild soil stress values. Consequently, plants adapt the hydraulic conductivity of their roots as well as that of the soil in their vicinity through exudates (Carminati and Javaux, 2020). Results from previous irrigation experiments using PRD or DI have shown that changes in stomatal conductance and shoot growth are some of the major components affected (Düring et al., 1996). In our experiment, the shoot growth fitted with the conventional leaf area and growth models, except at the end of the experiment when signs of water stress were visible on some leaves. The magnitude of the shoot growth is correlated with the number of roots. Drought may cause more inhibition of shoot growth than of root growth (Sharp and Davies, 1989). Although the root system was already well developed it is not possible to exclude its development as a factor influencing the CSD distribution.

(2) The spatiotemporal analysis of the ER showed that the water changes were not limited to root effects. Water redistribution from dry to wet in the soil and from shoot to dry roots (Smart et al., 2005, Lovisolo et al., 2016) may have occurred (Fig. A1 to A11). Additionally, even not visible from the screening face, capillary rise may have taken place due to the presence of a saturated zone at the bottom of the rhizotron. Due to the fact that water drained on both sides, RWU was not only vertically distributed but also horizontally. The range of water content varied significantly with a minimum SWC of about 0.25 m^3/m^3, repeatedly observed just before each irrigation meaning that the driest times are below field capacity conditions (estimated at 0.4 m^3/m^3). Drying half of the root system resulted in a reduction of the stomatal conductance (based on the mean of the distribution) of the order 5 mmol $m^{-2}s^{-1}$ after a 1 week cycle. Given the stress applied, the ER changes highlighted that root played a major role in the wine plant survival and evidenced strategies of adaptation. Indeed, the plant was able to adjust its water uptake and redistribution zones depending on the water availability, from all places, not only from the alternate irrigated areas.

641   (3) Finally, in order to know if the PRD conditions are met it would have been important not to

642   neglect the different states of root growth, and root renewal (because of renewal and decay) with

643   respect to the geophysical data. Nevertheless, this would have required opening and scanning the

644   rhizotron with conventional methods. Finally, we did not make a distinction between the hours of

645   the day although the changes observed for the irrigation are rapid, usually at the hourly scale, and

646   could be similar for RWU.

647
648

649   **4.4.   Performance of the acquisition protocol and the processing**

650

651   We discuss here how the quality of the recovered current density models by evaluating the performance of

652   the protocol and the processing. First, it is important to note that although the ERT data quality was good

653   (very few reciprocals were rejected, see Table A1), the inverted model was not perfect and this ultimately

654   has an impact also on the ECI forward model. The algorithm has undergone testing in a rhizotron

655   experiment and has demonstrated the ability to differentiate punctual sources, even when their current

656   contribution is as low as 5% of the total current (Peruzzo et al., 2020). The CSD resolution, of course,

657   matches the electrode interspace (in this case 5cm) and the smoothness constraint does not impact the

658   simulation of point source reconstruction. We adopted an inversion without any prior information to

659   recover the current density. Only model smoothing was applied by weighting the model data by an optimal

660   factor of 10 inferred from an L-curve analysis. Similar to the ERT inversion, the CSD problem is also ill-

661   posed. In this case, the 4-electrodes setup ensures that the current will flow through the plant after

662   injection, regardless of the contact resistance. However, the accuracy of the measured data may be

663   impacted by contact resistance, as errors in the measured resistance will negatively affect the quality of

664   ERT and CSD inversions. The impact is more pronounced on CSD, as it is dependent on ERT. Lastly,

665   because the box is relatively small and no-current-flow boundary conditions (Neumann) are imposed, we

666   may expect an effect due to the position of the return electrode where the current is attracted due to the

667   strongest gradient nearby (Mary et al., 2019b).

668

669

670   **4.5.   Outlook**

671   In order to strictly correlate PRD effects with geophysical measurements, one should consider a physical

672   barrier to separate the two sides of the rhizotron to a split-roots configuration. Another option is to increase

673   the lateral size to prevent redistribution or to use a very percolating material such as glass beads, gravels or

674   coarse sands. This should be carefully considered, as the rhizotron must also be an environment where

675   plant growth is possible under "natural" conditions, and for this some water retention capacity is needed

676   for the soil. A larger drainage capacity would simplify the interpretation as no-water redistribution from

677   one side to the other can occur. Although considering a barrier is technically possible, it would require a

678   more complex inversion scheme of the ERT and ECI considering that no electrical current can flow from

679   side to side. One could also consider increasing the measurement frequency to catch processes at an

680   hourly scale and comparing day/night measurements, particularly those associated with water

681   redistribution from the stem back to the roots at night when transpiration is reduced and its effect on the

682   water status of the roots. As we have seen that most of the water changes occurred in the day consecutive

683   to the irrigation, catching rapid changes of ER would help drive a conclusion on how much ECI is

684   connected to the active root zone. Finally, in order to draw robust statistical conclusions, the experiments

685   should be replicated for multiple plant samples.

686 **5. Conclusion**

687 The study aimed at understanding the current path in the root system and active root zones using geoelectrical imaging,

688 considering soil water content and irrigation regimes. Electrical Resistivity Tomography (ERT) is sensitive to both irrigation

689 and RWU processes. The ECI model uses a physical approach to measure current density after stem stimulation. The CSD

690   was very different from the control soil injection to the stem injection but nevertheless did not correlate with PRD cycles as

691   originally expected. We demonstrate that under mild stress conditions, it is practically impossible to spatially distinguish the

692   PRD effects using the ECI. We only evidenced that the Current Source Density distribution varied during the course of the

693   experiment considering evaporative demand but without any significant relationship to the Soil Water Content changes . A

694   few aspects of the experiment would gain to be more closely studied such as the water redistribution that possibly also

695   affects current distribution. In the future, we expect to improve our understanding by coupling the geophysical experiment

696   with an unsaturated soil-plant-atmosphere model.

697   **6.   Appendices**

698   **Appendix A: Time-lapse ERT inversion results**

699   As we selected only one cycle in the manuscript, we report here further details about the time-lapse ERT inversion results for

700   all the cycles. The inversion procedure is equivalent to the one described in Sect. 2.6.1 of the manuscript (Data processing -

701   Analysis of the ERT data). All time-lapse inversion models are plotted with a unique scale ranging from -20 to 20% of
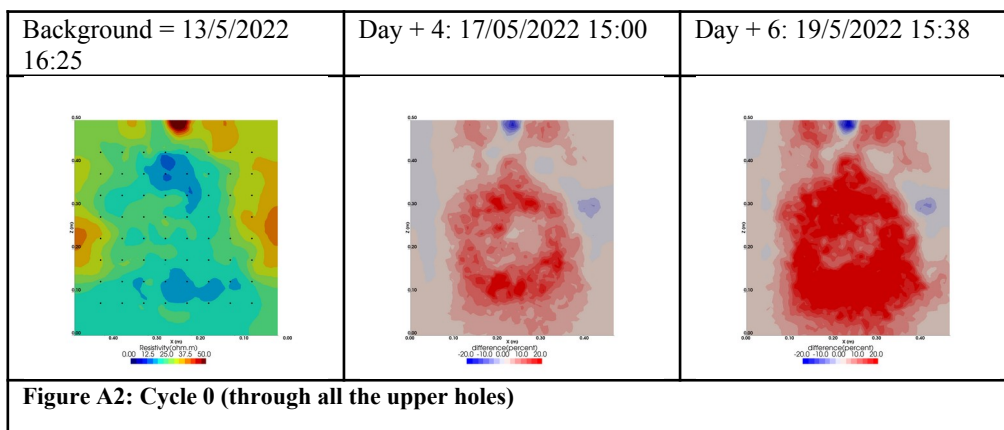
702   changes.

703

704
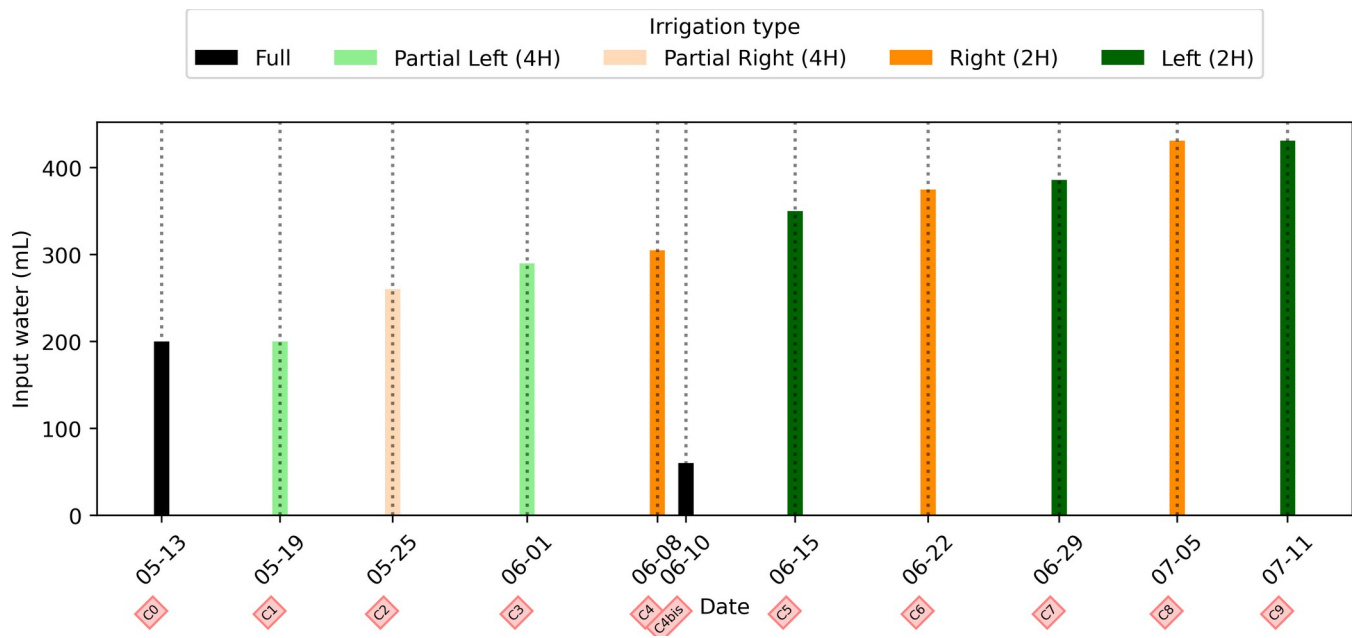
705

706

707

708

709 **Figure A1: Evolution of the quantity (in mL) of water input spatially distributed with an alternate between left (green) and right**
710 **(orange) during the PRD irrigation. The black bars hold for full-width irrigation (over all the holes, see fig. 1 manuscript), light**
711 **green and orange bars hold for irrigation over the 4 sides of holes, and dark green/orange for 2 holes irrigation.**
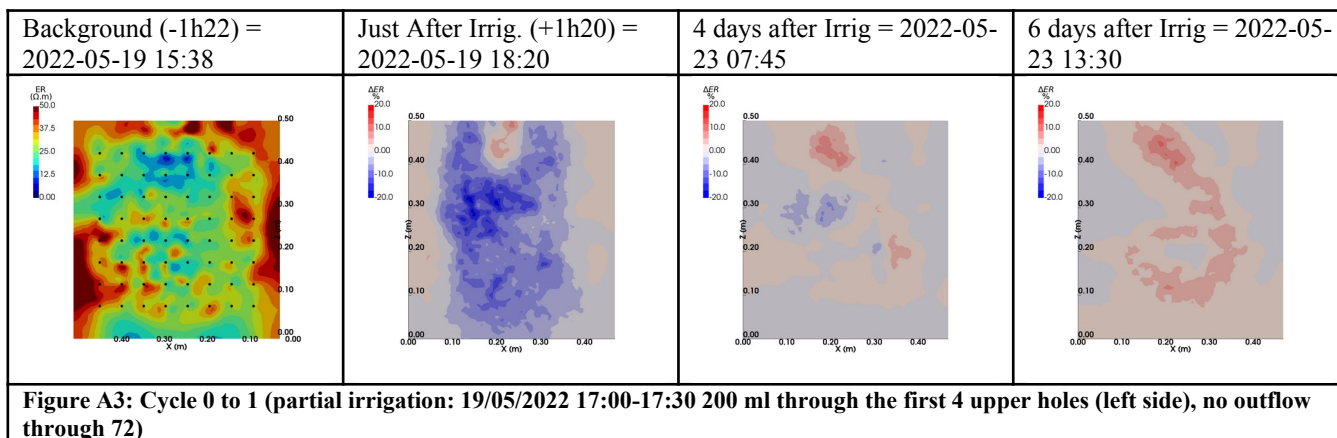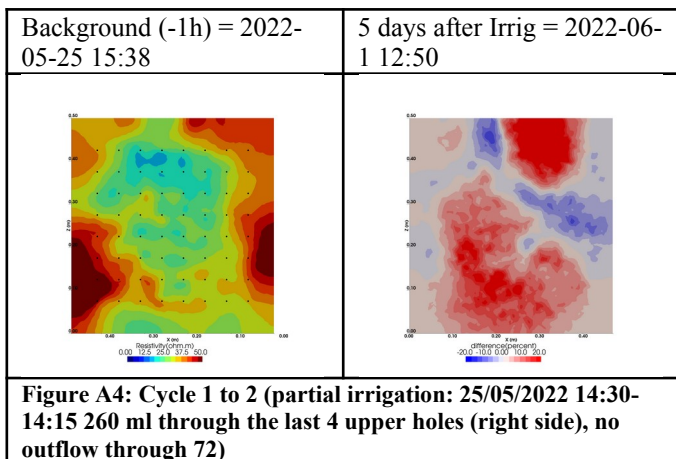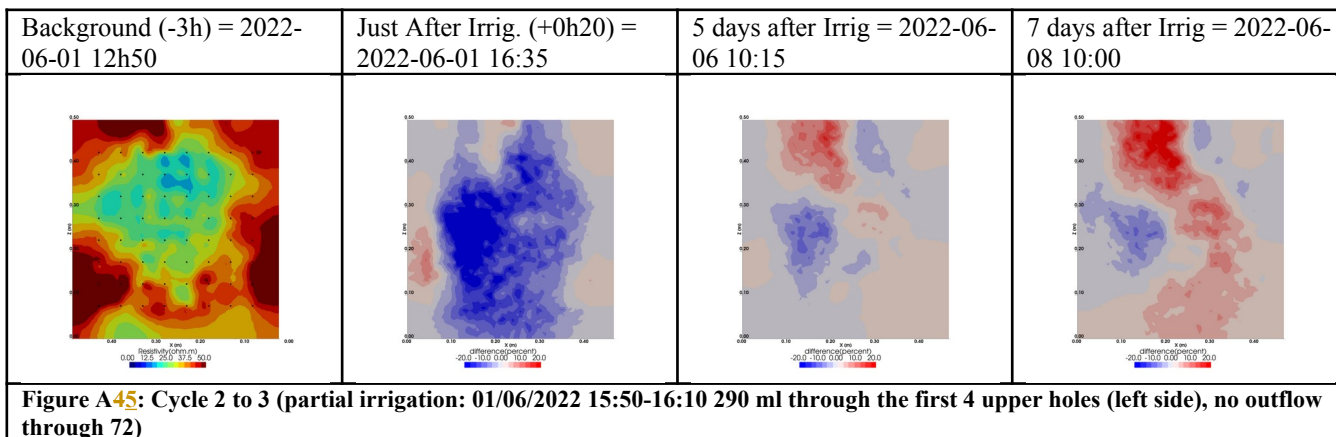
712

713

714

Background = 13/5/2022 16:25	Day + 4: 17/05/2022 15:00	Day + 6: 19/5/2022 15:38
Figure A2: Cycle 0 (through all the upper holes)		

715

716

Background (-1h22) = 2022-05-19 15:38	Just After Irrig. (+1h20) = 2022-05-19 18:20	4 days after Irrig = 2022-05-23 07:45	6 days after Irrig = 2022-05-23 13:30
Figure A3: Cycle 0 to 1 (partial irrigation: 19/05/2022 17:00-17:30 200 ml through the first 4 upper holes (left side), no outflow through 72)			

717
718

101
102

719
720

Background (-1h) = 2022-05-25 15:38	5 days after Irrig = 2022-06-1 12:50
Figure A4: Cycle 1 to 2 (partial irrigation: 25/05/2022 14:30-14:15 260 ml through the last 4 upper holes (right side), no outflow through 72)	

721
722
723

Background (-3h) = 2022-06-01 12h50	Just After Irrig. (+0h20) = 2022-06-01 16:35	5 days after Irrig = 2022-06-06 10:15	7 days after Irrig = 2022-06-08 10:00
Figure A45: Cycle 2 to 3 (partial irrigation: 01/06/2022 15:50-16:10 290 ml through the first 4 upper holes (left side), no outflow through 72)			

724
725
726

727

728

729

730

Background (-1h50) = 2022-06-08 10:00	Just After Irrig. (+0h30) = 2022-06-08 12:30
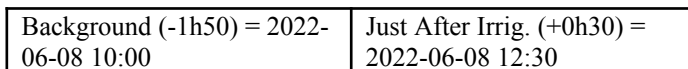
105
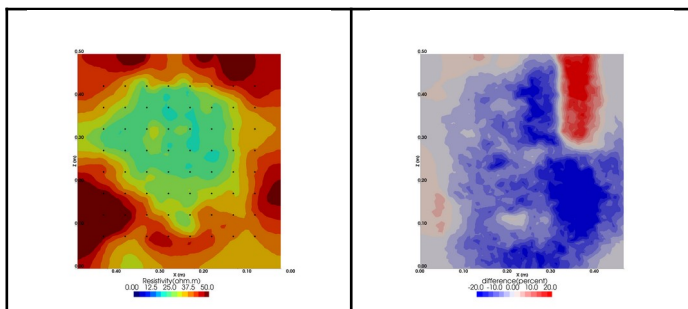
Figure A56: Cycle 3 to 4 (partial irrigation: 08/06/2022 11:50-12:00 305 ml through the last 2 upper holes (right side))

731

Background (-1h05) = 2022-06-15 16:20	Just After Irrig. (+1h) = 2022-06-15 17:50	7 days after Irrig = 2022-06-22 16:10
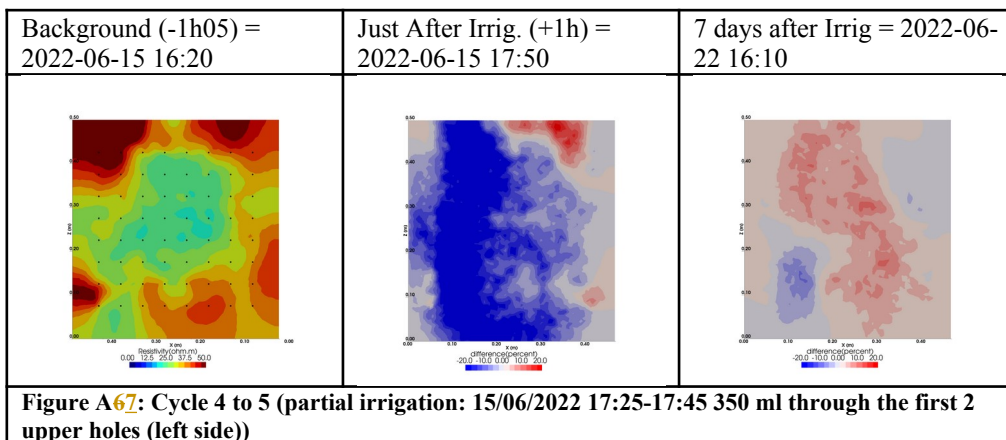
Figure A67: Cycle 4 to 5 (partial irrigation: 15/06/2022 17:25-17:45 350 ml through the first 2 upper holes (left side))

732

733

734

735

736

737

738

739

740

741

Background (-0h35) = 2022-06-22 16:10	Just After Irrig. (+0h30) = 2022-06-22 17h21	17h after Irrig = 2022-06-23 10:55	1 day after Irrig = 2022-06-23 15:20	6 days after Irrig = 2022-06-29 9:30
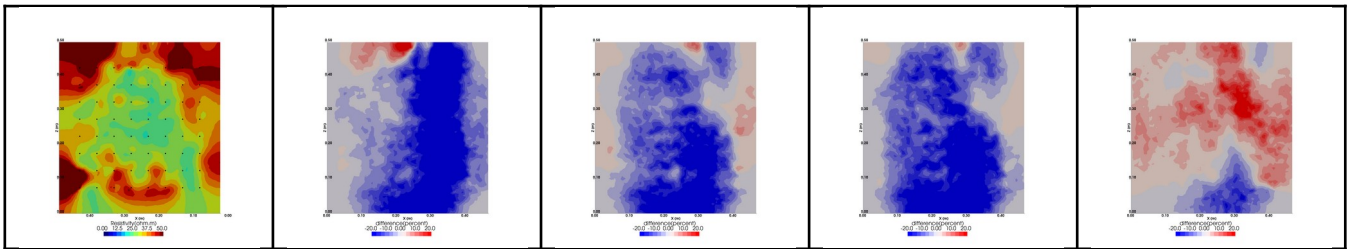
Figure A78: Cycles 5 and 6 time-lapse inversion (partial right side irrigation 22/06/2022 16:45-17:00, 375 ml)

742

743
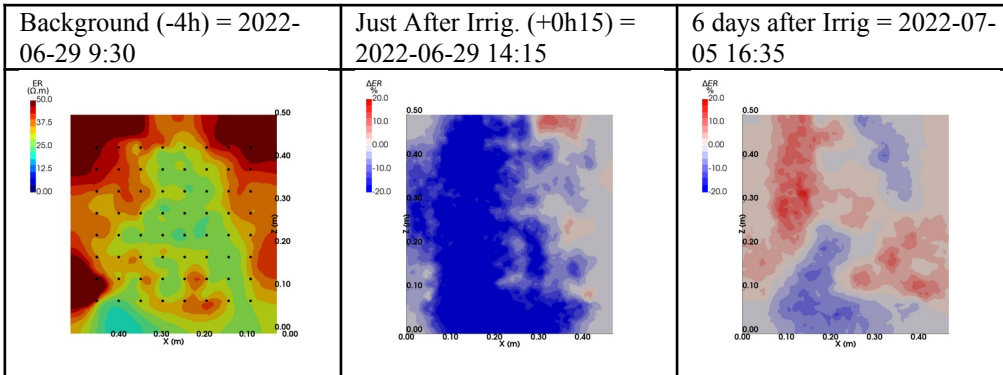
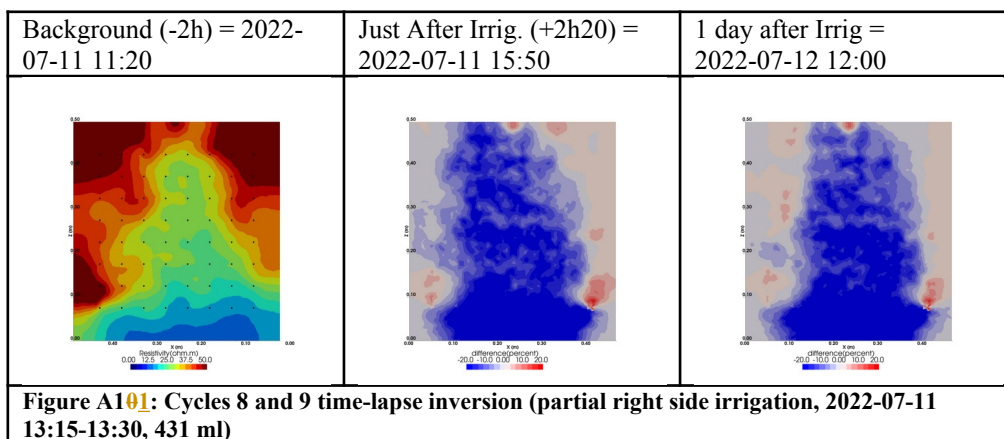**Figure A89: Cycles 6 and 7 time-lapse inversion (partial left side irrigation, 2022-06-29 13:45-14:00, 386 ml)**

744

745

746

Background (-3h) = 2022-07-05 16:35	Just After Irrig. (+0h) = 2022-07-05 18:25	2 days after Irrig = 2022-07-07 13:15	6 days after Irrig = 2022-07-11 11:20

Figure A910: Cycles 7 and 8 time-lapse inversion (partial right side irrigation, 2022-07-05 18:10-18:25, 431 ml)

747
748
749

Background (-2h) = 2022-07-11 11:20	Just After Irrig. (+2h20) = 2022-07-11 15:50	1 day after Irrig = 2022-07-12 12:00

Figure A101: Cycles 8 and 9 time-lapse inversion (partial right side irrigation, 2022-07-11 13:15-13:30, 431 ml)

750
751
752
753
754
755
756
757
758

Date	RMS (%)	# measurements read (over 2484)
2022-06-01 12:50:00	1.36	2048
2022-06-01 16:35:00	1.15	1920
2022-06-06 10:15:00	1.53	2268

2022-06-08 10:00:00	1.41	2230
2022-06-08 12:30:00	1.16	2028
2022-06-15 16:20:00	1.08	2137
2022-06-15 17:50:00	1.47	1493
2022-06-22 16:10:00	1.38	2109
2022-06-22 17:21:00	1.14	1372
2022-06-23 10:55:00	1.48	2229
2022-06-23 15:20:00	1.38	2268
2022-06-29 09:30:00	1.27	2075
2022-06-29 14:15:00	2.04	2027
2022-07-05 16:35:00	1.7	2067
2022-07-05 18:25:00	1.85	980
2022-07-07 13:15:00	1.98	2225
2022-07-11 11:20:00	2.5	2093
2022-07-11 15:50:00	2.72	2238
2022-07-12 12:00:00	2.68	2255

759   **Table A1: Table summarising the final RMS and the number of data used for each individual inversion**

760

761

762

763   **Appendix B: Inversion of current density (CSD)**

764

765   As we selected only one cycle in the manuscript, we report here further details about the time-lapse CSD inversion results
766   for all the cycles. The inversion procedure is equivalent to the one described in Sect. 2.6.2 of the manuscript (Data
767   processing - Analysis of current density) and we invite the reader to refer to Peruzzo et al. (2020) for a full description of the
768   algorithm. Furthermore, we extend the analysis showing the effect of the model regularisation (smoothing). Figures B1 and
769   B2 show the current density evolution with the time respectively for the stem and the soil injection with a regularisation
770   parameter of 1. The same is for Figures B3 and B4 with a regularisation of 10.

Figure B1: variations of the CSD for all the time steps (all cycles) during the stem injection. Inversion is unconstrained; data-model weighting factor (wr) is set to 1.
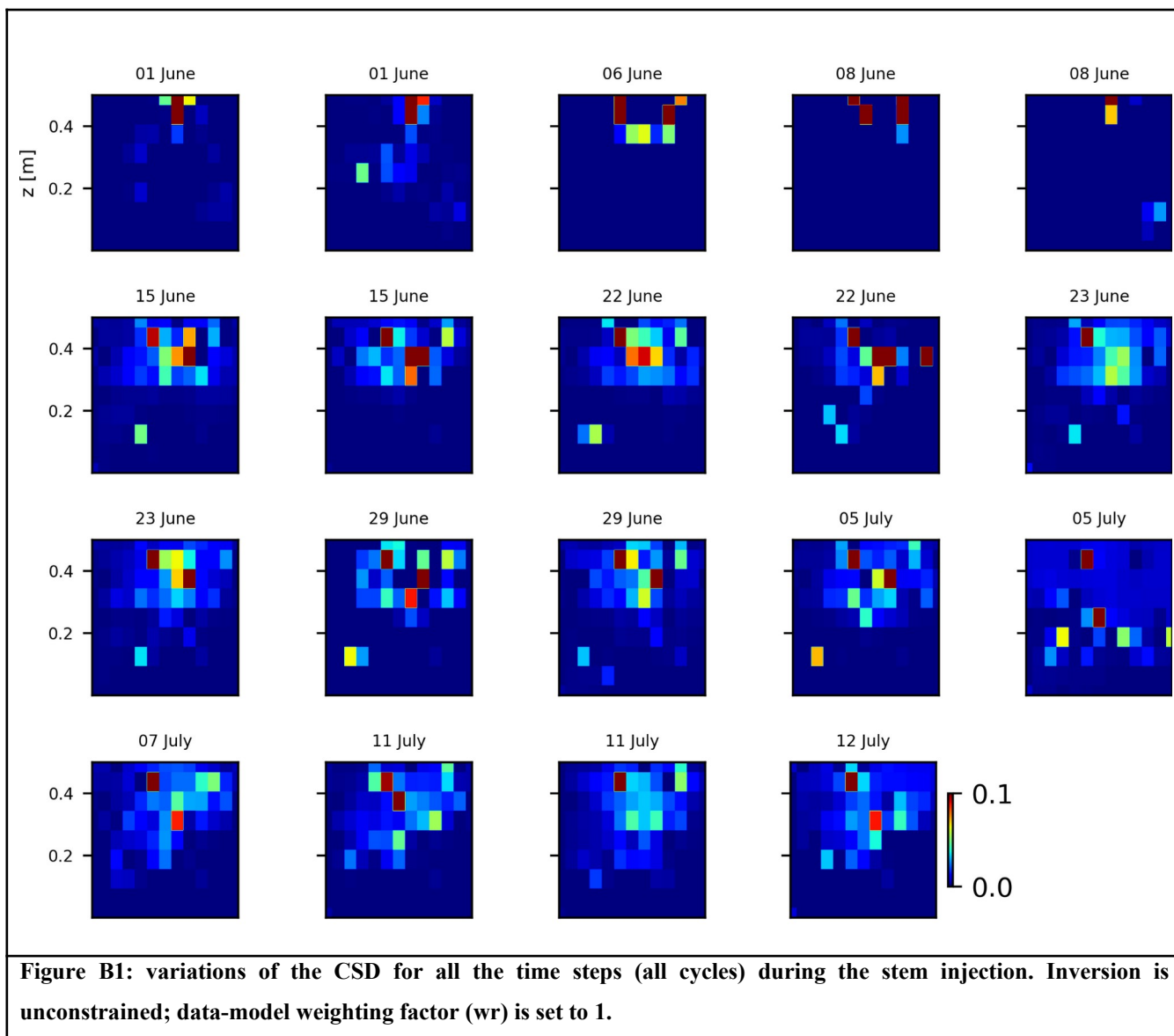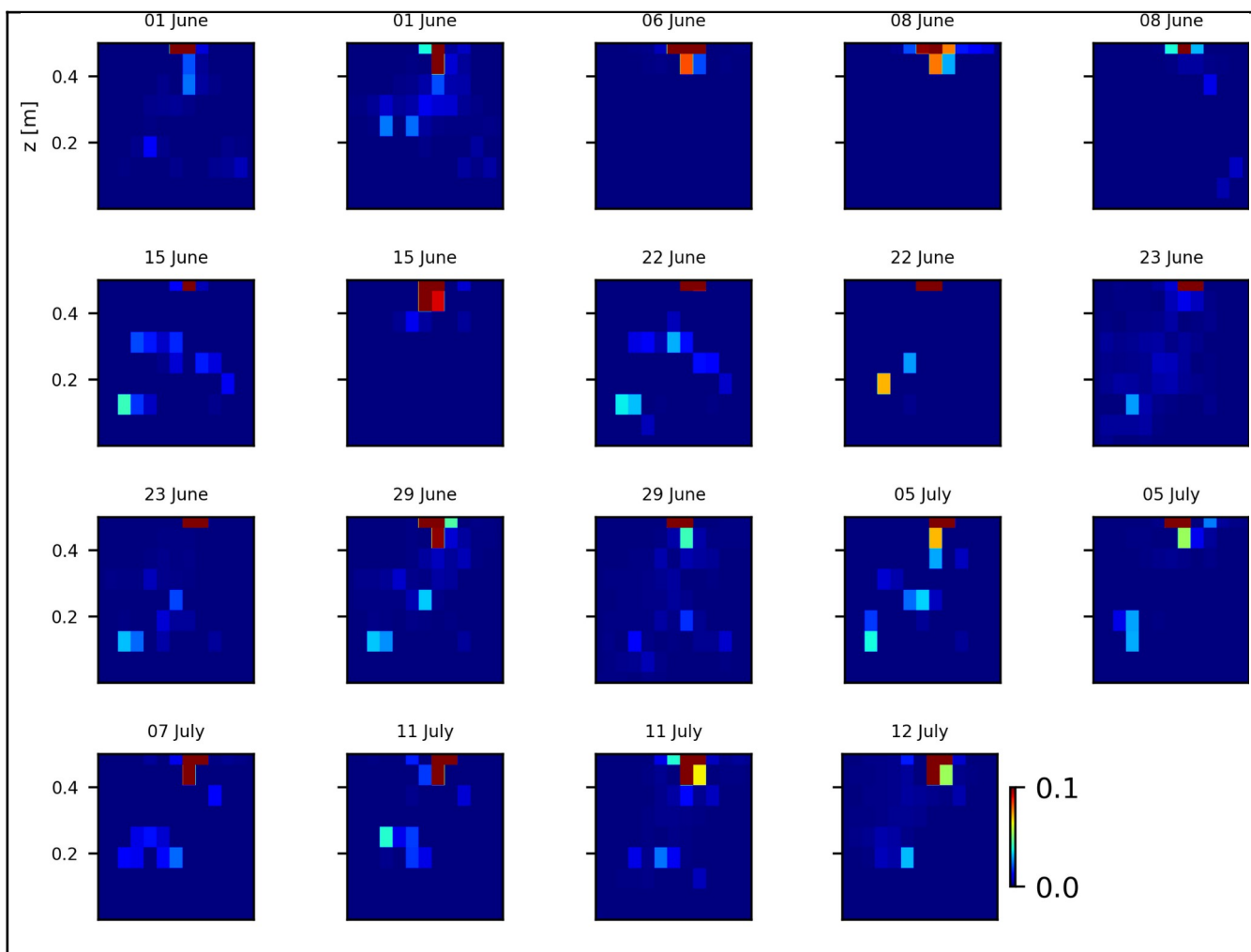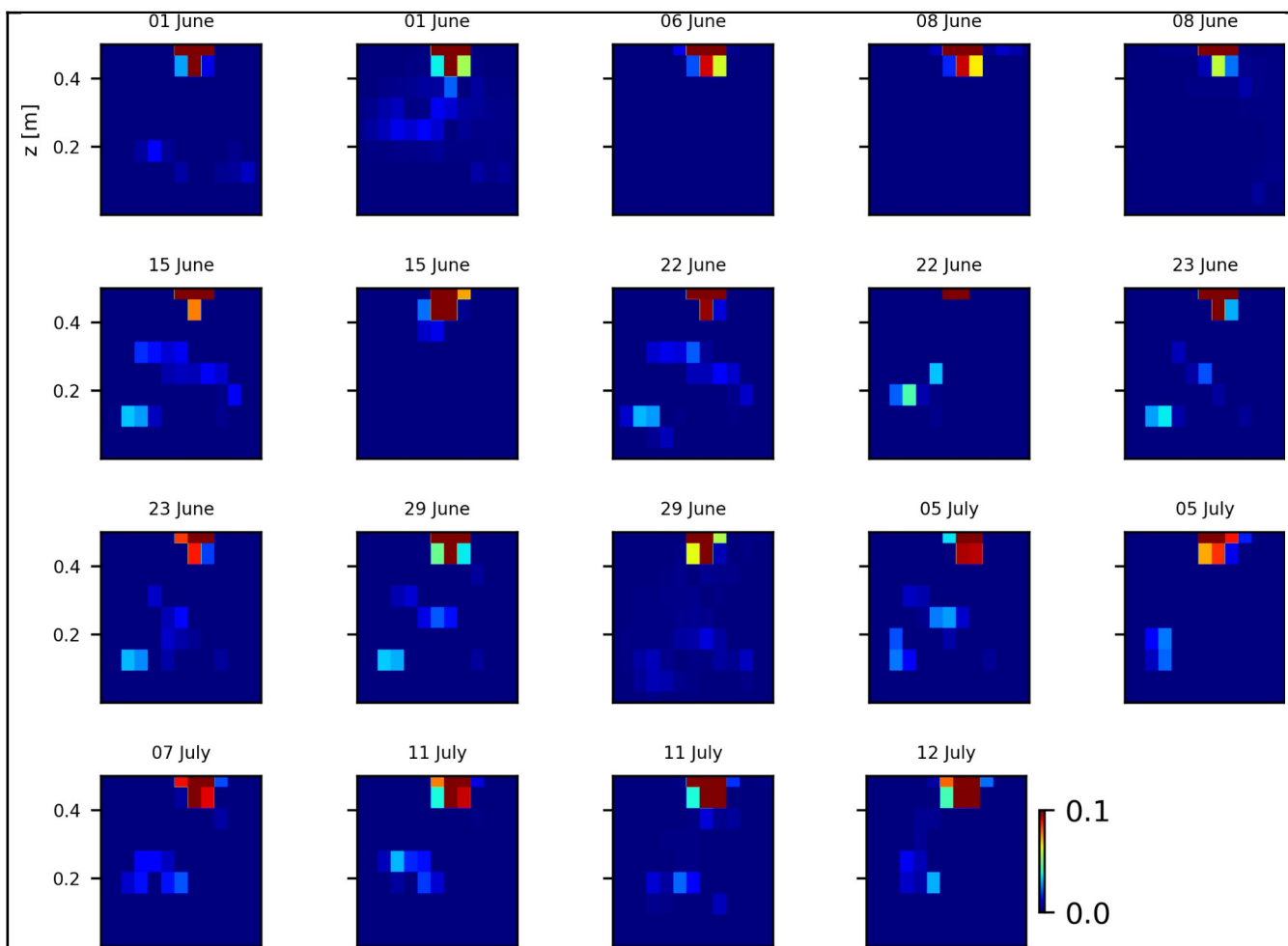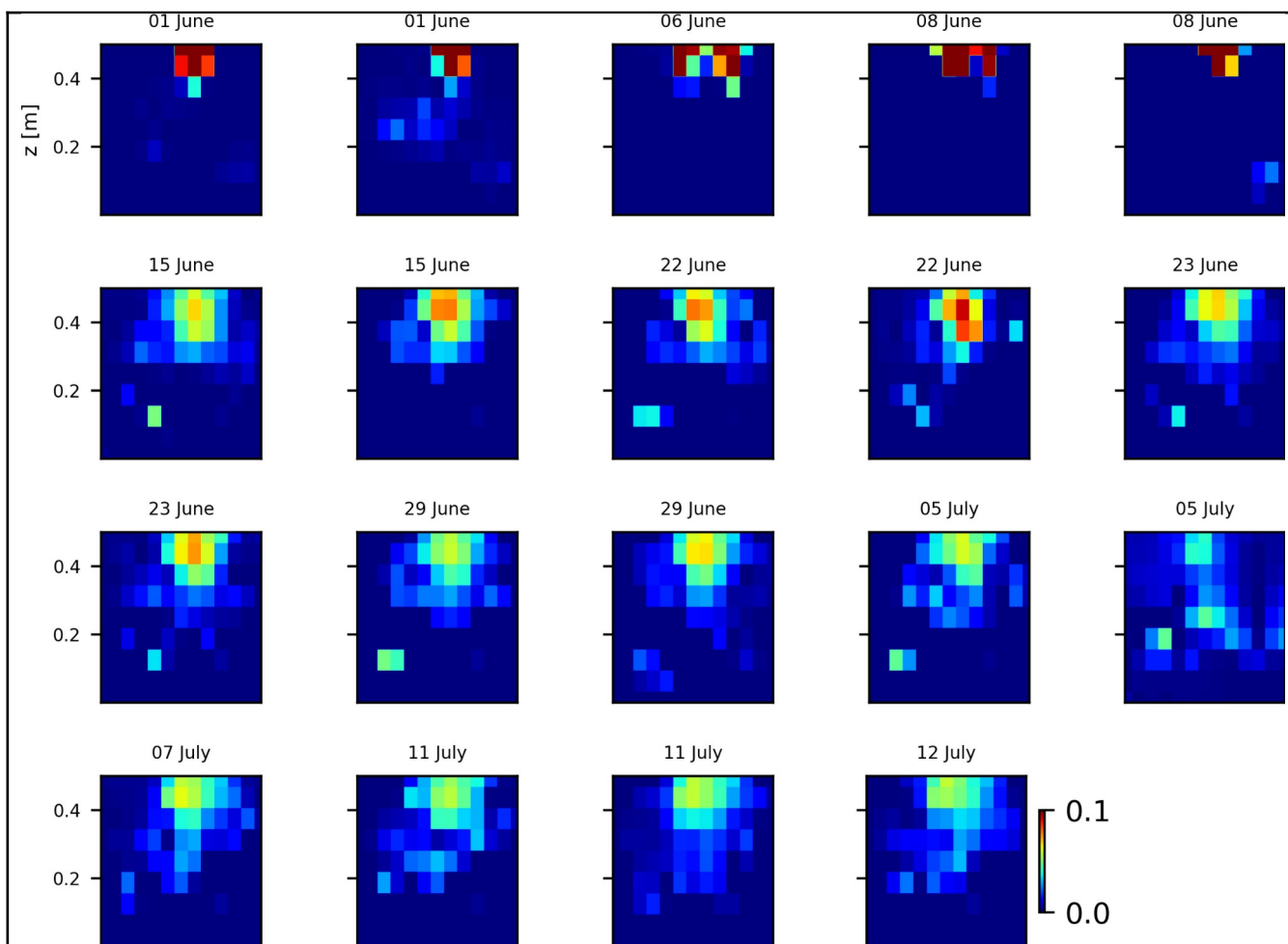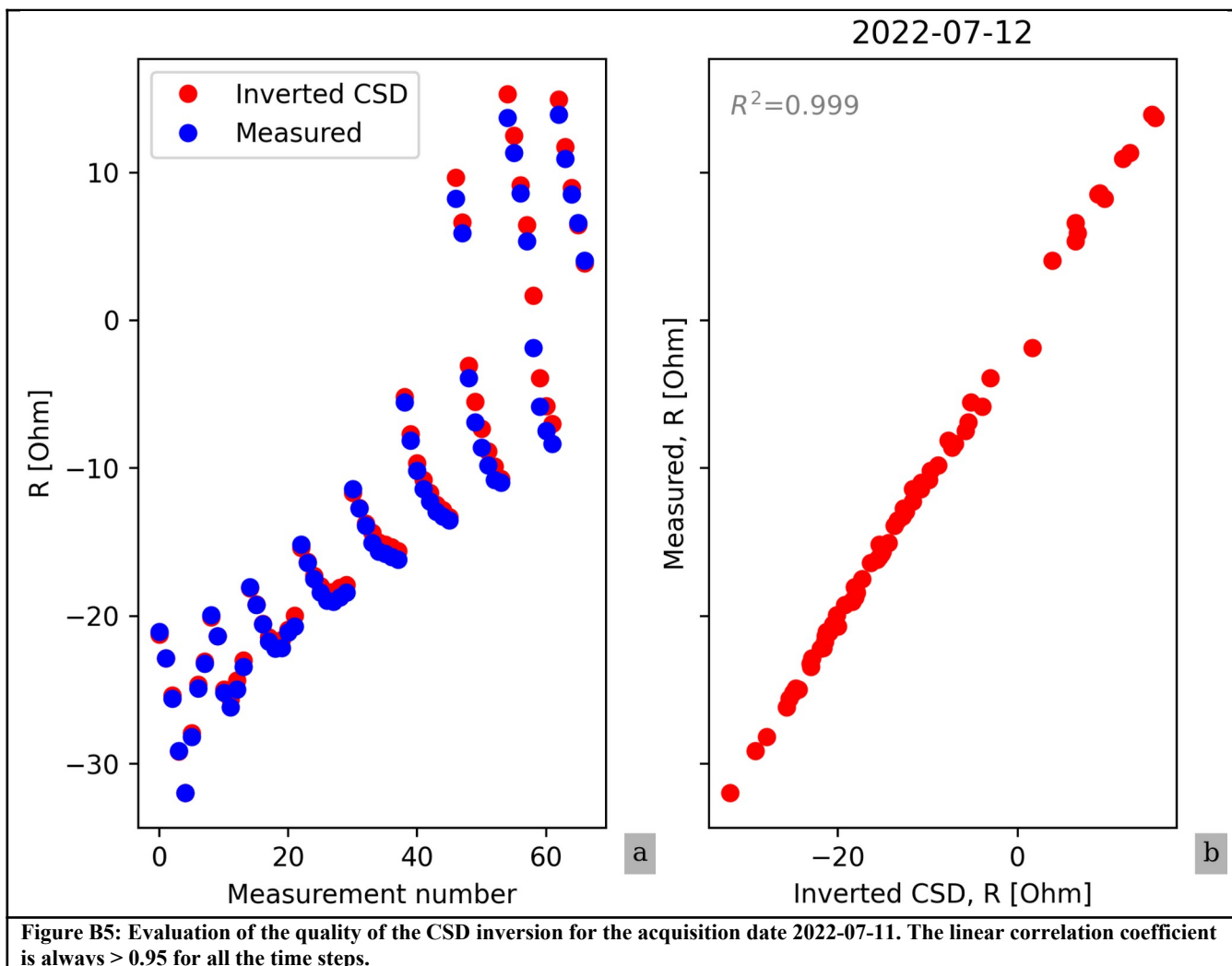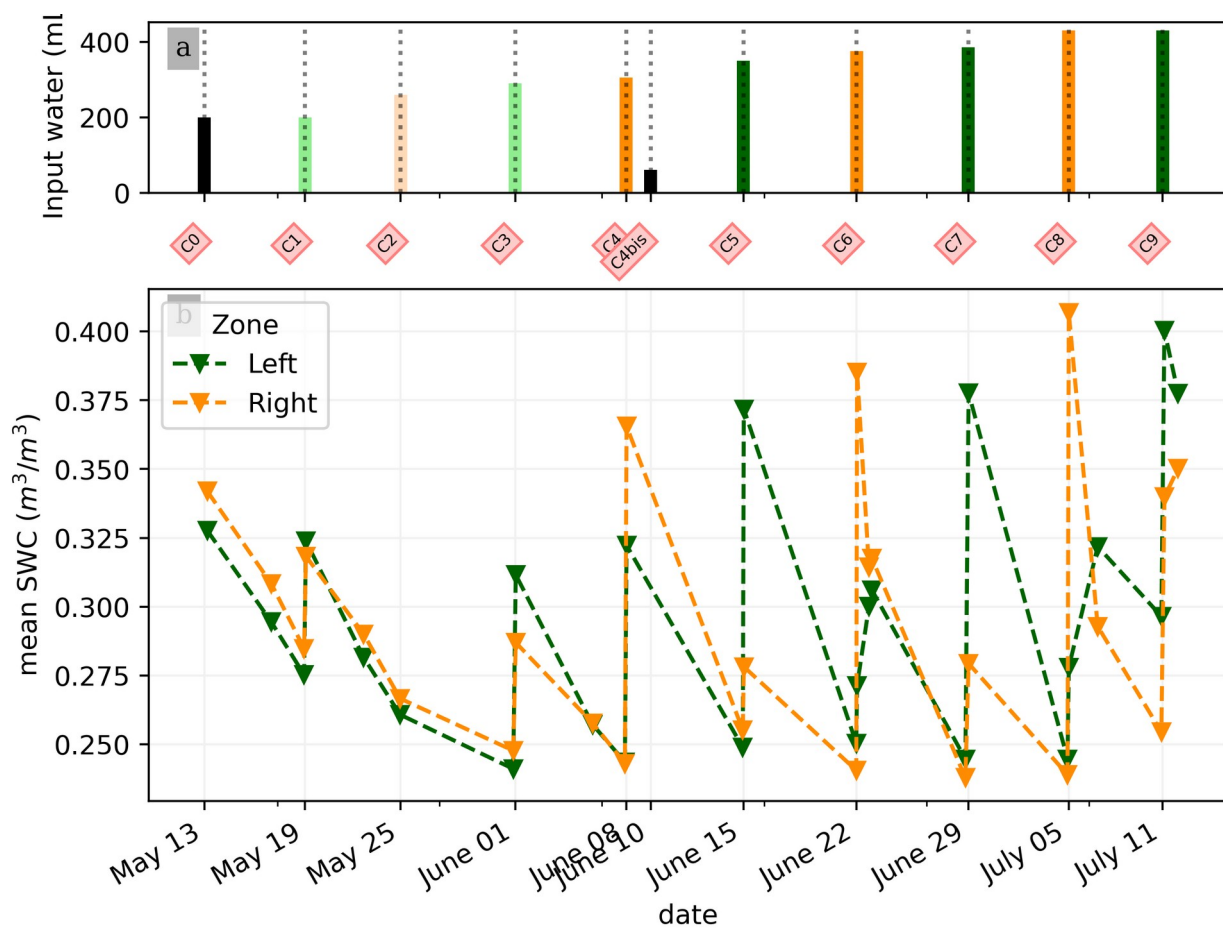
Figure B2: variations of the CSD for all the time steps (all cycles) during the soil control injection. Inversion is unconstrained; data-model weighting factor (wr) is set to 1.

773

774

775

776

777

Figure B3: variations of the CSD for all the time steps (all cycles) during the soil control injection. Inversion is unconstrained; data-model weighting factor (wr) is set to 10.

Figure B4: variations of the CSD for all the time steps (all cycles) during the stem injection. Inversion is unconstrained; data-model weighting factor (wr) is set to 10.

780

781

782

783

Figure B5: Evaluation of the quality of the CSD inversion for the acquisition date 2022-07-11. The linear correlation coefficient is always > 0.95 for all the time steps.

784

785

786

787   **Appendix C: Soil Water Content converted variations**

788

789

790

Figure C1: (a) Evolution of the quantity (in mL) of water input spatially distributed with an alternate between left (green) and right (orange) during the PRD irrigation. The black bars hold for full-width irrigation (over all the holes, see fig. 1 manuscript), light green and orange bars hold for irrigation over the 4 sides of holes, and dark green/orange for 2 holes irrigation. (b) Evolution of the mean SWC (m3/m3) average on each side, markers show the acquisition time.

7. Data availability

Codes and data to reproduce figures articles are available in the Zenodo data repository (link to come after decision).

References

1. Anonymous Reviewer: Comment on bg-2023-58, https://doi.org/10.5194/bg-2023-58-RC2, n.d.

2. Archie, G. E.: The Electrical Resistivity Log as an Aid in Determining Some Reservoir Characteristics, Trans. AIME, 146, 54–62, https://doi.org/10.2118/942054-G, 1942.

3. Binley, A.: 11.08 - Tools and Techniques: Electrical Methods, in: Treatise on Geophysics (Second Edition), edited by: Schubert, G., Elsevier, Oxford, 233–259, https://doi.org/10.1016/B978-0-444-53802-4.00192-5, 2015.

820   4. Binley, A. and Slater, L.: Resistivity and induced polarization: theory and applications to the near-surface earth,

821   Cambridge University Press, Cambridge, UK ; New York, NY, 2020.

822   5. Blanchy, G., Saneiyan, S., Boyd, J., McLachlan, P., and Binley, A.: ResIPy, an intuitive open source software for

823   complex geoelectrical inversion/modeling, Comput. Geosci., 137, 104423,

824   https://doi.org/10.1016/j.cageo.2020.104423, 2020.

825   6. Carminati, A. and Javaux, M.: Soil Rather Than Xylem Vulnerability Controls Stomatal Response to Drought,

826   Trends Plant Sci., 25, 868–880, https://doi.org/10.1016/j.tplants.2020.04.003, 2020.

827   7. Cassiani, G., Boaga, J., Vanella, D., Perri, M. T., and Consoli, S.: Monitoring and modelling of soil–plant

828   interactions: the joint use of ERT, sap flow and eddy covariance data to characterize the volume of an orange tree

829   root zone, Hydrol. Earth Syst. Sci., 19, 2213–2225, https://doi.org/10.5194/hess-19-2213-2015, 2015.

830   8. Cassiani, G., Boaga, J., Rossi, M., Putti, M., Fadda, G., Majone, B., and Bellin, A.: Soil–plant interaction monitoring:

831   Small scale example of an apple orchard in Trentino, North-Eastern Italy, Science of The Total Environment, 543,

832   851–861, https://doi.org/10.1016/j.scitotenv.2015.03.113, 2016.

833   9. Collins, M., Fuentes, S., and Barlow, E.: Partial rootzone drying and deficit irrigation increase stomatal sensitivity

834   to vapour pressure deficit in anisohydric grapevines, Funct Plant Biol, 37, 129–138, 2009.

835   10. Consoli, S., Stagno, F., Vanella, D., Boaga, J., Cassiani, G., and Roccuzzo, G.: Partial root-zone drying irrigation in

836   orange orchards: Effects on water use and crop production characteristics, European Journal of Agronomy, 82, 190–

837   202, https://doi.org/10.1016/j.eja.2016.11.001, 2017.

838   11. Cseresnyés, I., Vozáry, E., Kabos, S., and Rajkai, K.: Influence of substrate type and properties on root electrical

839   capacitance, Int. Agrophysics, 34, 95–101, https://doi.org/10.31545/intagr/112147, 2020.

840   12. Dalton, F. N.: In-situ root extent measurements by electrical capacitance methods, Plant Soil, 173, 157–165,

841   https://doi.org/10.1007/BF00155527, 1995.

842   13. Dietrich, S., Carrera, J., Weinzettel, P., and Sierra, L.: Estimation of Specific Yield and its Variability by Electrical

843   Resistivity Tomography, Water Resour. Res., 54, 8653–8673, https://doi.org/10.1029/2018WR022938, 2018.

140
141

844 14. Doussan, C. and Garrigues, E.: Measuring and Imaging the Soil-root-water System with a Light Transmission 2D
845   Technique, Bio-Protocol, 9, https://doi.org/10.21769/BioProtoc.3190, 2019.

846 15. Düring, H., Dry, P. R., Botting, D. G., and Loveys, B.: Effects of partial root-zone drying on grapevine vigour,
847   yield, composition of fruit and use of water, in: Proceedings of the Ninth Australian Wine Industry Technical
848   Conference : Adelaide, South Australia, 16-19 july 1995, 1996, págs. 128-131, Proceedings of the Ninth Australian
849   Wine Industry Technical Conference : Adelaide, South Australia, 16-19 july 1995, 128–131, 1996.

850 16. Ehosioke, S., Nguyen, F., Rao, S., Kremer, T., Placencia-Gomez, E., Huisman, J. A., Kemna, A., Javaux, M., and
851   Garré, S.: Sensing the electrical properties of roots: A review, Vadose Zone J., 19, e20082,
852   https://doi.org/10.1002/vzj2.20082, 2020.

853 17. Elsner, E. A. and Jubb, G. L.: Leaf Area Estimation of Concord Grape Leaves from Simple Linear Measurements,
854   Am. J. Enol. Vitic., 39, 95–97, 1988.

855 18. Garré, S., Javaux, M., Vanderborght, J., Pagès, L., and Vereecken, H.: Three-dimensional electrical resistivity
856   tomography to monitor root zone water dynamics, Vadose Zone Journal, 10, 412–424,
857   https://doi.org/10.2136/vzj2010.0079, 2011.

858 19. Garré, S., Hyndman, D., Mary, B., and Werban, U.: Geophysics conquering new territories: The rise of
859   "agrogeophysics," Vadose Zone J., 20, e20115, https://doi.org/10.1002/vzj2.20115, 2021.

860 20. Garrigues, E., Doussan, C., and Pierret, A.: Water Uptake by Plant Roots: I – Formation and Propagation of a Water
861   Extraction Front in Mature Root Systems as Evidenced by 2D Light Transmission Imaging, Plant Soil, 283, 83–98,
862   https://doi.org/10.1007/s11104-004-7903-0, 2006.

863 21. Geuzaine, C. and Remacle, J.-F.: Gmsh: A 3-D finite element mesh generator with built-in pre- and post-processing
864   facilities, Int. J. Numer. Methods Eng., 79, 1309–1331, https://doi.org/10.1002/nme.2579, 2009.

865 22. Gibert, D., Le Mouël, J.-L., Lambs, L., Nicollin, F., and Perrier, F.: Sap flow and daily electric potential variations
866   in a tree trunk, Plant Science, 171, 572–584, https://doi.org/10.1016/j.plantsci.2006.06.012, 2006.

867   23. Gimenez, C., Gallardo, M., and Thompson, R. B.: PLANT–WATER RELATIONS, in: Encyclopedia of Soils in the

868   Environment, edited by: Hillel, D., Elsevier, Oxford, 231–238, https://doi.org/10.1016/B0-12-348530-4/00459-8,

869   2005.

870   24. Gu, H., Liu, L., Butnor, J., Sun, H., Zhang, X., Li, C., and Liu, X.: Electrical capacitance estimates crop root traits

871   best under dry conditions—a case study in cotton (Gossypium hirsutum L.), Plant Soil, 467, 1–19,

872   https://doi.org/10.1007/s11104-021-05094-6, 2021.

873   25. Hoagland, D. R. and Arnon, D. I. (1950). The water culture method for growing plants without soil. California

874   Agric Exp Stn Circ 347: 1-32.

875   26. Jackisch, C., Knoblauch, S., Blume, T., Zehe, E., and Hassler, S. K.: Estimates of tree root water uptake from soil

876   moisture profile dynamics, Biogeosciences, 17, 5787–5808, https://doi.org/10.5194/bg-17-5787-2020, 2020.

877   27. Kamarajan, C., Pandey, A. K., Chorlian, D. B., and Porjesz, B.: The use of current source density as

878   electrophysiological correlates in neuropsychiatric disorders: a review of human studies, Int. J. Psychophysiol. Off.

879   J. Int. Organ. Psychophysiol., 97, 310–322, https://doi.org/10.1016/j.ijpsycho.2014.10.013, 2015.

880   28. Liu, Y., Li, D., Qian, J., Di, B., Zhang, G., and Ren, Z.: Electrical impedance spectroscopy (EIS) in plant roots

881   research: a review, Plant Methods, 17, https://doi.org/10.1186/s13007-021-00817-3, 2021.

882   29. Lovisolo, C., Lavoie-Lamoureux, A., Tramontini, S., and Ferrandino, A.: Grapevine adaptations to water stress:

883   new   perspectives   about   soil/plant   interactions,   Theor.   Exp.   Plant   Physiol.,   28,   53–66,

884   https://doi.org/10.1007/s40626-016-0057-7, 2016.

885   30. Malavasi, U. C., Davis, A. S., and Malavasi, M. de M.: Lignin in Woody Plants under Water Stress: A Review,

886   Floresta E Ambiente, 23, 589–597, https://doi.org/10.1590/2179-8087.143715, 2016.

887   31. Michot, D., Benderitter, Y., Dorigny, A., Nicoullaud, B., King, D., and Tabbagh, A.: Spatial and temporal

888   monitoring of soil water content with an irrigated corn crop cover using surface electrical resistivity tomography:

889   Soil Water Study Using Electrical Resistivity, Water Resour. Res., 39, https://doi.org/10.1029/2002WR001581,

890   2003.

891   32. Mancuso, S. (Ed.): Measuring roots: an updated approach, Springer, Heidelberg ; New York, 382 pp., 2012.

33. Martin-Vertedor, A. I. and Dodd, I. C.: Root-to-shoot signalling when soil moisture is heterogeneous: increasing the proportion of root biomass in drying soil inhibits leaf growth and increases leaf abscisic acid concentration: Root distribution and non-hydraulic signalling, Plant Cell Environ., 34, 1164–1175, https://doi.org/10.1111/j.1365-3040.2011.02315.x, 2011.

34. Mary, B., Peruzzo, L., Boaga, J., Schmutz, M., Wu, Y., Hubbard, S. S., and Cassiani, G.: Small-scale characterization of vine plant root water uptake via 3-D electrical resistivity tomography and mise-à-la-masse method, Hydrol. Earth Syst. Sci., 22, 5427–5444, https://doi.org/10.5194/hess-22-5427-2018, 2018.

35. Mary, B., Vanella, D., Consoli, S., and Cassiani, G.: Assessing the extent of citrus trees root apparatus under deficit irrigation via multi-method geo-electrical imaging, Sci. Rep., 9, 9913, https://doi.org/10.1038/s41598-019-46107-w, 2019a.

36. Mary, B., Rao, S., Javaux, M., and Cassiani, G.: Tree root system mise-à-la-masse (MALM) forward modelling with explicit representation of root structure., in: Geophysical Research Abstracts, 2019b.

37. McAdam, S. A. M., Sussmilch, F. C., and Brodribb, T. J.: Stomatal responses to vapour pressure deficit are regulated by high speed gene expression in angiosperms, Plant Cell Environ., 39, 485–491, https://doi.org/10.1111/pce.12633, 2016.

38. Parsekian, A. D., Claes, N., Singha, K., Minsley, B. J., Carr, B., Voytek, E., Harmon, R., Kass, A., Carey, A., Thayer, D., and Flinchum, B.: Comparing Measurement Response and Inverted Results of Electrical Resistivity Tomography Instruments, J. Environ. Eng. Geophys., 22, 249–266, https://doi.org/10.2113/JEEG22.3.249, 2017.

39. Peruzzo, L., Chou, C., Wu, Y., Schmutz, M., Mary, B., Wagner, F. M., Petrov, P., Newman, G., Blancaflor, E. B., Liu, X., Ma, X., and Hubbard, S.: Imaging of plant current pathways for non-invasive root Phenotyping using a newly developed electrical current source density approach, Plant Soil, 450, 567–584, https://doi.org/10.1007/s11104-020-04529-w, 2020.

40. Peruzzo, L., Liu, X., Chou, C., Blancaflor, E. B., Zhao, H., Ma, X.-F., Mary, B., Iván, V., Weigand, M., and Wu, Y.: Three-channel electrical impedance spectroscopy for field-scale root phenotyping, Plant Phenome J., 4, e20021, https://doi.org/10.1002/ppj2.20021, 2021.

149
150

917 41. Postic, F. and Doussan, C.: Benchmarking electrical methods for rapid estimation of root biomass, Plant Methods,
918   12, 33, https://doi.org/10.1186/s13007-016-0133-7, 2016.

919 42. Rao, S., Meunier, F., Ehosioke, S., Lesparre, N., Kemna, A., Nguyen, F., Garré, S., and Javaux, M.: A mechanistic
920   model for electrical conduction in soil–root continuum: a virtual rhizotron study, Biogeochemistry: Land,
921   https://doi.org/10.5194/bg-2018-280, 2018.

922 43. Sartoni, R., Zegada-Lizarazu, W., and Monti, A.: A new compartmentalised rhizotron system for root phenotyping,
923   Ital. J. Agron., 10, 53, https://doi.org/10.4081/ija.2015.645, 2015.

924 44. Sharp, R. E. and Davies, W. J.: Regulation of growth and development of plants growing with a restricted supply of
925   water, Semin. Ser. - Soc. Exp. Biol., 1989.

926 45. Smart, D. R., Carlisle, E., Goebel, M., and Nunez, B. A.: Transverse hydraulic redistribution by a grapevine, Plant
927   Cell Environ, 28, 157–166, https://doi.org/10.1111/j.1365-3040.2004.01254.x, 2005.

928 46. Song, C., Shen, W., Du, L., Wen, J., Lin, J., and Li, R.: Development and chemical characterization of Casparian
929   strips in the roots of Chinese fir (Cunninghamia lanceolata), Trees, 33, 827–836, https://doi.org/10.1007/s00468-
930   019-01820-x, 2019.

931 47. Stoll, M.: Effects of partial rootzone drying on grapevine physiology and fruit quality, 2000.

932 48. Stoll, M., Loveys, B., and Dry, P.: Hormonal changes induced by partial rootzone drying of irrigated grapevine,
933   Journal of Experimental Botany, 51, 1627–1634, https://doi.org/10.1093/jexbot/51.350.1627, 2000.

934 49. Taylor, H. M., Upchurch, D. R., and McMichael, B. L.: Applications and limitations of rhizotrons and
935   minirhizotrons for root studies, Plant Soil, 129, 29–35, https://doi.org/10.1007/BF00011688, 1990.

936 50. Tsialtas, J. T., Koundouras, S., and Zioziou, E.: Leaf area estimation by simple measurements and evaluation of leaf
937   area prediction models in Cabernet-Sauvignon grapevine leaves, Photosynthetica, 46, 452–456,
938   https://doi.org/10.1007/s11099-008-0077-x, 2008.

939 51. Tsukanov, K. and Schwartz, N.: Relationship between wheat root properties and its electrical signature using the
940   spectral induced polarization method, Vadose zone j., 19, https://doi.org/10.1002/vzj2.20014, 2020.

152
153

941   52. Tsukanov, K. and Schwartz, N.: Modeling Plant Roots Spectral Induced Polarization Signature, Geophys. Res.

942   Lett., 48, e2020GL090184, https://doi.org/10.1029/2020GL090184, 2021.

943   53. Uhlemann, S., Wilkinson, P. B., Maurer, H., Wagner, F. M., Johnson, T. C., and Chambers, J. E.: Optimized survey

944   design for electrical resistivity tomography: combined optimization of measurement configuration and electrode

945   placement, Geophys. J. Int., 214, 108–121, https://doi.org/10.1093/gji/ggy128, 2018.

946   54. Urban, J., Bequet, R., and Mainiero, R.: Assessing the applicability of the earth impedance method for in situ

947   studies of tree root systems, J. Exp. Bot., 62, 1857–1869, https://doi.org/10.1093/jxb/erq370, 2011.

948   55. Vanella D., G. Cassiani, L. Busato, J. Boaga, S. Barbagallo, A. Binley, S. Consoli, 2018, Use of small scale

949   electrical resistivity tomography to identify soil-root interactions during deficit irrigation, *Journal of Hydrology*,

950   556, 310-324, doi: 10.1016/j.jhydrol.2017.11.025.

951   56. Virtanen, P., Gommers, R., Oliphant, T. E., Haberland, M., Reddy, T., Cournapeau, D., Burovski, E., Peterson, P.,

952   Weckesser, W., Bright, J., van der Walt, S. J., Brett, M., Wilson, J., Millman, K. J., Mayorov, N., Nelson, A. R. J.,

953   Jones, E., Kern, R., Larson, E., Carey, C. J., Polat, İ., Feng, Y., Moore, E. W., VanderPlas, J., Laxalde, D., Perktold,

954   J., Cimrman, R., Henriksen, I., Quintero, E. A., Harris, C. R., Archibald, A. M., Ribeiro, A. H., Pedregosa, F., and

955   van Mulbregt, P.: SciPy 1.0: fundamental algorithms for scientific computing in Python, Nat. Methods, 17, 261–

956   272, https://doi.org/10.1038/s41592-019-0686-2, 2020.

957   57. Voytek, E. B., Barnard, H. R., Jougnot, D., and Singha, K.: Transpiration- and precipitation-induced subsurface

958   water flow observed using the self-potential method, Hydrol. Process., https://doi.org/10.1002/hyp.13453, 2019.

959   58. Whalley, W. R., Binley, A., Watts, C. W., Shanahan, P., Dodd, I. C., Ober, E. S., Ashton, R. W., Webster, C. P.,

960   White, R. P., and Hawkesford, M. J.: Methods to estimate changes in soil water for phenotyping root activity in the

961   field, Plant Soil, 415, 407–422, https://doi.org/10.1007/s11104-016-3161-1, 2017.

962   59. Weigand, M.: Monitoring Structural And Physiological Properties Of Crop Roots Using Spectral Electrical

963   Impedance Tomography, University of Bonn, 2017.

964   60. Weigand, M. and Kemna, A.: Imaging and functional characterization of crop root systems using spectroscopic

965   electrical impedance measurements, Plant Soil, 435, 201–224, https://doi.org/10.1007/s11104-018-3867-3, 2019.

966   61. Yan, J., Bogie, N. A., and Ghezzehei, T. A.: Root uptake under mismatched distributions of water and nutrients in

967   the root zone, Biogeosciences, 17, 6377–6392, https://doi.org/10.5194/bg-17-6377-2020, 2020.